The interplay of rifting, magmatism and formation of geothermal resources in the Ethiopian Rift constrained by 3-D magnetotelluric imaging

Marie Luise Texas Dambly[1], Friedemann Samrock[1], Alexander Grayver[2], and Martin O. Saar[1]

[1]ETH Zurich
[2]University of Cologne,ETH Zurich

December 7, 2022

Abstract

The Main Ethiopian Rift (MER) is accompanied by extensive volcanism and the formation of geothermal systems, both having an imminent impact on lives of millions of local inhabitants. Although previous studies from the region found evidence that asthenospheric upwelling and associated decompression melting provide melt to magmatic mush systems that feed the tectono-volcanic segments in the rift valley, no geophysical model imaged these regional and local scale transcrustal structures within a single comprehensive 3-D model. To fill this gap, we combined regional and local magnetotelluric data sets to obtain the first multi-scale 3-D electrical conductivity model of the central MER. The model clearly images a magma ponding zone with up to 7 vol.% melt at the base of the crust in the western part of the rift, its connection to Aluto volcano via a tectonically controlled transcrustal magmatic mush system and how the melt, stored at shallow crustal depths, supplies heat for Aluto's geothermal system. Our model provides evidence that different volcano-tectonic lineaments in the rift valley share a common melt source, which has been debated in the past. The presented multi-scale model provides new constraints as well as geologic insights into the melt distribution below the rift and will facilitate future geothermal developments and volcanic hazard assessments in the MER.

The interplay of rifting, magmatism and formation of geothermal resources in the Ethiopian Rift constrained by 3-D magnetotelluric imaging

M.L.T. Dambly[1], F. Samrock[1], A. V. Grayver[2,3], M. O. Saar[1,4]

[1]Geothermal Energy and Geofluids group, Institute of Geophysics, Department of Earth Sciences, ETH Zurich, Sonneggstrasse 5, 8092 Zurich, Switzerland
[2]Earth and Planetary Magnetism group, Institute of Geophysics, Department of Earth Sciences, ETH Zurich, Sonneggstrasse 5, 8092 Zurich, Switzerland
[3]Institute of Geophysics and Meteorology, University of Cologne, Albertus-Magnus-Platz, 50923 Cologne, Germany
[4]Department of Earth and Environmental Sciences, University of Minnesota, 55455 Minneapolis, USA

Key Points:

- First 3-D multi-scale magnetotelluric model images the entire transcrustal tectono-magmatic system below the Main Ethiopian Rift.
- A lower crustal magma ponding zone feeds a fault controlled magmatic mush system providing heat for the geothermal system of Aluto volcano.
- Eastern and western volcano-tectonic lineaments share a common lower crustal magma source with an estimated melt fraction of 7 percent.

Corresponding author: Marie Luise Texas Dambly, `mdambly@ethz.ch`

Abstract

The Main Ethiopian Rift (MER) is accompanied by extensive volcanism and the formation of geothermal systems, both having an imminent impact on lives of millions of local inhabitants. Although previous studies from the region found evidence that asthenospheric upwelling and associated decompression melting provide melt to magmatic mush systems that feed the tectono-volcanic segments in the rift valley, no geophysical model imaged these regional and local scale transcrustal structures within a single comprehensive 3-D model. To fill this gap, we combined regional and local magnetotelluric data sets to obtain the first multi-scale 3-D electrical conductivity model of the central MER. The model clearly images a magma ponding zone with up to 7 vol. % melt at the base of the crust in the western part of the rift, its connection to Aluto volcano via a tectonically controlled transcrustal magmatic mush system and how the melt, stored at shallow crustal depths, supplies heat for Aluto's geothermal system. Our model provides evidence that different volcano-tectonic lineaments in the rift valley share a common melt source, which has been debated in the past. The presented multi-scale model provides new constraints as well as geologic insights into the melt distribution below the rift and will facilitate future geothermal developments and volcanic hazard assessments in the MER.

Plain Language Summary

Continental rifting is a fundamental process of plate tectonics that breaks continents apart to ultimately form new oceans. The landscape of the Main Ethiopian Rift (MER) is characterized by abundant volcanism and hot springs, which indicate presence of geothermal resources formed by magmatic heating of subsurface water. In our study we present a 3-D subsurface image of the magmatic system and geothermal reservoir beneath Aluto volcano in the MER. The model shows the electrical conductivity distribution of the subsurface which allows us to infer the distribution of electrically conductive melt. This is the first model that provides a high-resolution image of the entire magmatic system below the MER from the deep magmatic melt source up to the surface. The new model images for the first time how geothermal reservoirs form as a consequence of rifting related volcanic activity thereby providing a clear illustration of fundamental geological processes. These results also have a high societal relevance by providing a basis for volcanic risk assessment and contributing to a better understanding of how the sustainable green geothermal energy resources form.

1 Introduction

The East African Rift System (EARS) is a prominent continental rift that shaped the landscape of East Africa, including the East African Plateau, rift valleys and numerous volcanoes. Rifting and rift-related volcanism in East Africa played a role in early human evolution (King & Bailey, 2006) and to this date affect the life of humans due to volcanic hazards (Biggs et al., 2021), but also by providing diverse climate conditions and rift-associated natural resources (Burnside et al., 2021; Kebede et al., 2020). A large number of studies, especially in the northern part of the EARS, the Main Ethiopian Rift (MER), have provided a wealth of information and knowledge on the geodynamic processes that initiated and drive rifting and associated volcanism in the EARS (e.g. Agostini et al., 2011a; Casey et al., 2006; Corti, 2009; Ebinger, 2005; Kendall et al., 2005; Kendall & Lithgow-Bertelloni, 2016; Keranen & Klemperer, 2008, and references therein).

One of the main findings of these studies is that neither mechanical stretching nor magmatic upwelling could be the the major driver of rifting alone, but it is a rather complex interplay between these processes (e.g. Beutel et al., 2010; Kendall et al., 2005). Active magmatism and volcanism in the MER is sustained by asthenospheric upwelling. The main hypothesis is that decompression melting occurs in the upper mantle, melt intrudes into the lithosphere, where it feeds magmatic dykes and sills leading to the formation of volcanic systems in the MER (Gallacher et al., 2016; Rychert et al., 2012). Petrological studies and geological mapping (Bonini et al., 2005; Keranen & Klemperer, 2008) from the central part of the MER (CMER) observed a correlation between the monogenetic vent distribution and fault systems (Fig. 1), which implies that a tectono-magmatic interplay drives the rifting. Multiple studies proposed that a complex magmatic system exists below the western, mostly aseismic, Silti Debre Zeyit Fault Zone (SDFZ) (Iddon & Edmonds, 2020; Mazzarini et al., 2013; Rooney et al., 2011), where the magma stalls and fractionates at multiple depths within the crust. In contrast, the eastern Wonji Fault Belt (WFB) is seismically more active (Keir et al., 2006), hosting most of the present-day crustal extension with well-developed magmatic pathways (Bilham et al., 1999; Mazzarini et al., 2013; Rooney et al., 2011). Magma rises quickly under the WFB and fractionates at low pressures corresponding to about 5 km depth (Gleeson et al., 2017; Iddon & Edmonds, 2020; Rooney et al., 2011). Along the WFB, long-lived silicic peralkaline volcanoes are found with shallow magma chambers that have undergone several phases of eruption and recharge (Fontijn et al., 2018). Active magmatism and extensional strain along the WFB created ideal geological conditions for the formation of high-temperature geothermal resources (e.g. Jolie et al., 2021).

However, there is still a lack of geophysical subsurface models for the MER that would constrain the 3-D distribution of melt and image magmatic pathways across the continental crust. Such geophysical subsurface images are critical for understanding controls on magma transport, magma emplacement under rift-aligned segments and the formation of numerous magma-driven geothermal systems in the MER (e.g. Jolie et al., 2021; Kebede et al., 2020). The mindful exploitation of these geothermal resources would be beneficial for the local society (IRENA, 2020). As a source of clean and renewable baseload energy, these geothermal resources can satisfy the growing energy demand and sustain the local economic growth. Numerous countries along the EARS plan to expand exploitation of renewable geothermal energy resources (IRENA, 2020). Ethiopia is currently aiming at installing 1000 MWe of its estimated 10.000 MWe geothermal energy potential (Burnside et al., 2021; Kebede et al., 2020).

Our study focuses on the area of Ethiopia's only producing geothermal power plant, Aluto-Langano. The power plant is in operation since 1998 and has an installed capacity of 7.3 MWe (Kebede et al., 2020). Expansion work to reach 75 MWe is underway, with four new wells having been drilled in 2022 (capitalethiopia.com, 2022). Our primary goal here is to investigate the magmatic heat source of Aluto's geothermal system and how it is connected to deeper lower crustal magmatic system. To this end, we will use the magnetotelluric (MT) method and image 3-D electrical conductivity structure of the subsurface.

Previous MT and seismic studies from this region have identified electrical conductivity and shear wave velocity anomalies in the lower crust under the SDFZ (Hübert et al., 2018; Kim et al., 2012; Samrock et al., 2015). These lower crustal seismic anomalies have been interpreted as the lithospheric melt ponding zone. However, the lateral extent of this anomaly and potential links to Aluto's magmatic reservoir under the WFB remain poorly constrained. Further, it remains unclear whether volcanoes along the WFB and the SDFZ are related to a common melt ponding zone or whether their magmas originate from separated parental melt sources (e.g. Fig. 11 in Mazzarini et al., 2013; Rooney et al., 2011).

To address these questions and better constrain the structure below Aluto, we analyzed a new MT dataset that covers both the rift and the Aluto volcanic complex. Our goal is to obtain a new multi-scale 3-D electrical conductivity model of this area in the CMER (Fig. 1)

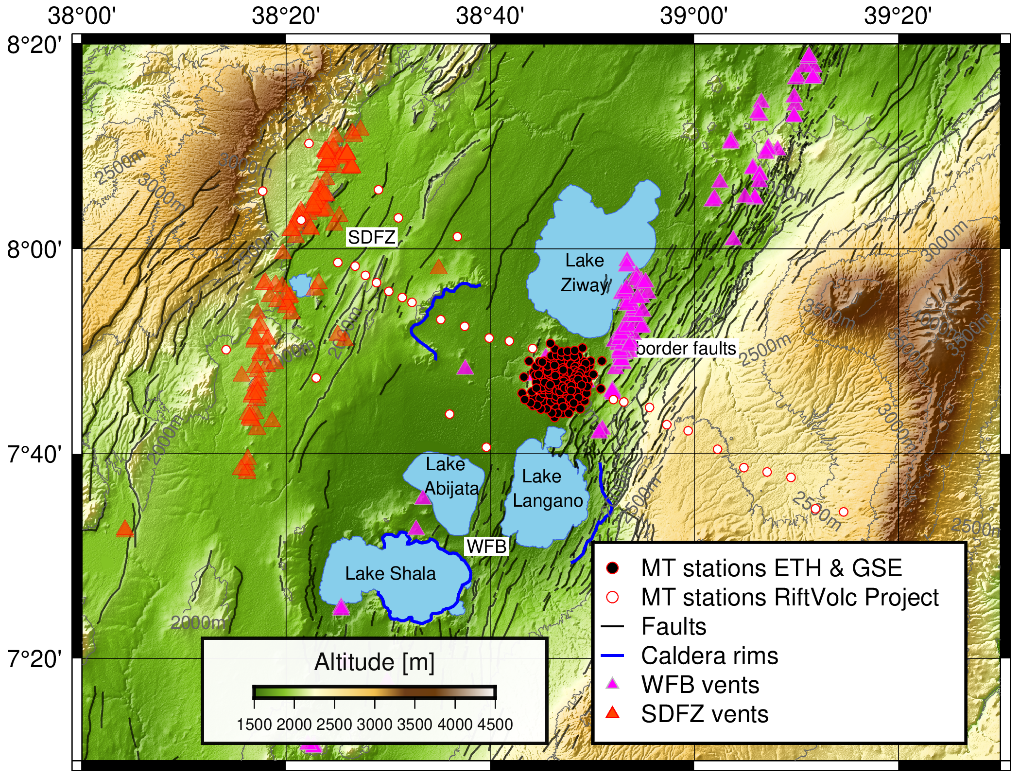

Figure 1. Study area in the Central Main Ethiopian Rift (CMER) with its faults systems (database of faults: Agostini et al., 2011b) and quaternary vents (grouped by Mazzarini & Isola, 2010). The vents belong to two different volcanic belts that are associated with the Wonji Fault Belt (WFB) and the Silti Debre Zeyit Fault Zone (SDFZ). Aluto volcano is located in the center of the study area in between the lakes Ziway and Langano. MT stations are coloured according to the institutions and projects that performed the measurement (MT-dataset by ETH Zurich (ETH) and Geological Survey of Ethiopia (GSE): Samrock et al. (2010) and MT-dataset by the RiftVolc Project: Hübert and Whaler (2020)). The survey area encompasses all fault systems of the CMER (WFB, SDFZ and border faults) and crosses the Gademotta caldera rim west of Aluto. The maximum difference in altitude along the profile is $\approx 1000\,\mathrm{m}$.

and resolve both regional-scale structures in the lower crust and local structures related to Aluto's upper crustal magmatic and geothermal reservoirs.

2 Method and Data

To image the melt distribution across the rift and constrain the structures of Aluto's magmatic and geothermal reservoirs, we obtain the subsurface 3-D electrical conductivity distribution employing the (passive) magnetotelluric method (MT) (e.g. Cagniard, 1953). Broadband MT responses are sensitive to electrical conductivity structures across a wide range of scales, providing a unique opportunity to study the subsurface from the surface down to the upper mantle. More details on the MT method are provided in the SI (Text S1).

2.1 Data

We combine data from regional and local MT surveys in the MER, as is shown in Fig. 1. The regional dataset, collected within the RiftVolc Project (Hübert & Whaler, 2020), consists of 33 MT stations that are distributed across the rift over a distance of 120 km with average site spacings between 4 km and 13 km (SI: Tab. S1). These regional-scale MT survey was supplemented by a local dataset of ETH and GSE (Samrock et al., 2010), consisting of 165 sites that cover the edifice of the Aluto volcano (15×15 km), with an average site spacing of 0.7 km. The MT transfer functions cover a period range of $T = 10^{-2} - 10^{3}$ s. For this period range and for the averaged electrical conductivity distribution in the study area, the penetration depth is calculated to range between 0.5 and 92.5 km, thereby providing a sufficient range for imaging both near-surface and crustal structures (SI: Fig. S2). Detailed information on the surveys and the collected MT data is provided in the SI (Text S2).

2.2 3-D Inversion

We used the GoFEM code to perform 3-D forward modelling and inversion (Arndt et al., 2020; Grayver, 2015; Grayver & Kolev, 2015). GoFEM uses locally refined meshes to facilitate multi-scale model parameterization (SI: Text S4) and accurately incorporate topography. The code was already used in earlier local-scale MT studies at Aluto (Samrock et al., 2020) and for multi-scale MT studies of volcanically active regions in Mongolia (Käufl et al., 2020).

Since impedance tensors are often affected by galvanic distortions, we first perform a phase tensor inversion. As the starting model for the phase tensor inversion, we used a homogeneous model with a resistivity of $\bar{\rho}^{1D}_{a,ssq} = 19.25\,\Omega$m, where $\bar{\rho}^{1D}_{a,ssq}$ is the geometric mean of all observed apparent resistivities calculated from Z_{ssq} (SI: Eq. 6-11, see also Rung-Arunwan et al., 2016).

Although phase tensors are free of galvanic distortions (e.g. Caldwell et al., 2004), absolute values of electrical conductivity in models constrained solely by phase tensor data might be less constrained, especially when survey layout is sparse (Tietze et al., 2015). To mitigate this limitation, we ran the impedance tensor inversion and used the best-fitting

3-D phase tensor model as a starting model. By doing so, the impedance tensor inversion is guided by the distortion-free phase tensor model and the negative impact of galvanic distortions on the inversion is reduced. If there were no distortions and both phase and impedance tensors contained the same information, we would expect the models to be identical. In reality, the models exhibit some differences, mostly because the impedance tensor inversion need to compensate for galvanic distortions by introducing some scattered conductivity structures at shallow depths (Fig. 2 Samrock et al., 2018) (SI: Fig. S13).

Technical information on the inversion methodology and the achieved data fit for the final phase and impedance tensor models is provided in the SI (Text S3 and S4). In what follows, we will present the final impedance tensor model. The corresponding phase tensor model is shown for completeness in the SI (Text S4.1).

3 Results

Both models, obtained from phase and impedance tensor inversions, fit the observed data within the uncertainty (RMS$\leq$1), given by the error-floor of 5 % applied row-wise to the impedance tensor and propagated to the phase tensor (as in Käufl et al., 2018). Details about the inversion progress and the achieved fit are provided in Fig. 2. Starting at an initial RMS of 2.7, the phase tensor inversion converges to an RMS of 0.83 within four iterations. For the subsequent impedance tensor inversion a relatively low model regularization is chosen, as the large-scale structure is given by the phase tensor model, which is used as the starting model for the impedance tensor inversion. Starting at an initial RMS of 5.1, the impedance tensor inversion converges progressively until a final RMS of 0.81 is achieved (Fig. 2a). The RMS distribution as a function of the period shows that shorter periods tend to yield lower misfits than longer periods (Fig. 2b), which can be due to lower data quality at longer periods. The normalized residuals of both obtained final models are uniformly distributed and centered around zero, indicating that no systematic bias is present (Fig. 2c). More detailed information about the model fit is provided in the SI (Text S5.2).

3.1 Final model

A cross-section through the final electrical conductivity model is shown in Fig. 3 a. An approximately NW-SE-oriented vertical slice crosses the entire rift and traverses the center

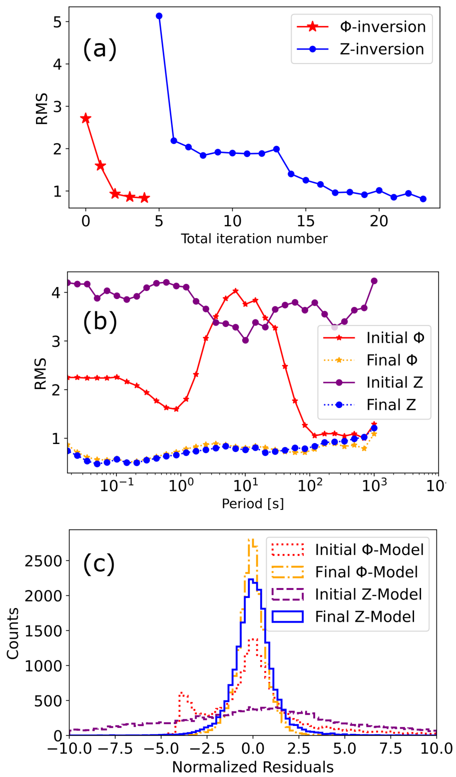

Figure 2. (a) RMS misfit during the phase tensor and the subsequent impedance tensor inversions. (b) RMS misfit versus period for the initial and final phase and impedance tensor inversion runs. (c) Residual distribution of initial and final phase tensor and impedance tensor models. Note that the final phase tensor model is used as a starting model for the impedance tensor inversion.

of Aluto volcano. Main electrical conductors (C) in the obtained multi-scale model are described in the following.

The largest conductivity anomaly in the model is the C3 conductor. The maximum recovered electrical conductivity within C3 is $\sigma = 0.18\,\mathrm{S/m}$ (Fig. 3 a). The anomaly occupies a large volume in the lower crust under the western part of the rift and crosses the Moho boundary at depths of $z \approx 30-35\,\mathrm{km}$ b.s.l. (Fig. 5). The lateral extent of C3 is about 50 km across the rift and 30 km along the rift, considering the $0.1\,\mathrm{S/m}$ isosurface (we note that data coverage along the rift axis is limited). It is evident that no high conductivity zone is found under the eastern part of the rift. C3 ends abruptly around the central rift axis and transitions into a continuously upward propagating channel denoted C2. The C2 structure is characterized by increased bulk electrical conductivities of $\sigma = 1.8\,\mathrm{S/m}$ at depths of $z = 6 - 18\,\mathrm{km}$ b.s.l.. This channel terminates at a depth of $z = 4\,\mathrm{km}$,b.s.l. right below the Aluto volcano (Fig. 3 b). At shallower depths (down to about $z \approx 1.5\,\mathrm{km}$ below surface), we

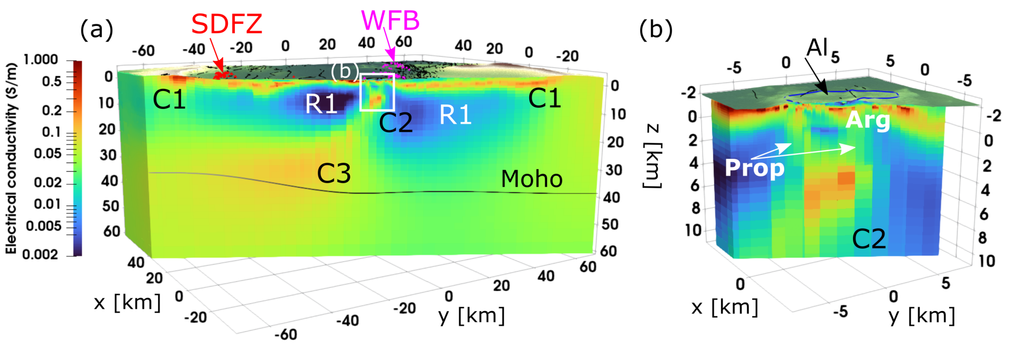

Figure 3. Final 3-D electrical conductivity model. (a) NW-SE oriented cross-section, covering the entire width of the CMER. The Moho boundary (black solid line) is taken from (Stuart et al., 2006). Pink and red triangles depict WFB and SDFZ vents, respectively (see also Fig. 1). Recovered structures are interpreted to be: (C1) Aquifer/sediment unit, (C2) magma ascent channel, (R1) solidified igneous rock and (C3) lower crustal melt ponding zone. The white box marks the area of the Aluto-Langano geothermal system (b). (b) Enlarged excerpt of the Aluto volcano (proposed caldera rim in blue). Increased conductivities in the shallow subsurface can be attributed to a clay cap, formed by argillic alteration (Arg) and higher-temperature propyllitic alteration (Prop).

recover an electrically conductive layer (C1) that extends across the entire width of the rift, with bulk conductivity values of $\sigma = 0.1 - 0.5\,\mathrm{S/m}$. This continuous layer (C1) is interrupted only under the edifice of Aluto volcano in the center of the shown cross-section (Fig. 3).

A large low-conductivity zone (R1) extends across the valley, with $\sigma \leq 0.01\,\mathrm{S/m}$. R1 is situated in the crust below the continuous conductive layer (C1) and is pierced by the conductive channel C2.

3.2 Interpretation

The presented electrical conductivity model is the first 3-D model of the CMER that images the transcrustal distribution of magma in sufficient detail to interpret it across scales from the lower crust to the surface. In what follows, we provide a geological interpretation of our 3-D electrical conductivity model (Figs. 3 and 5) taking in consideration earlier studies.

3.2.1 C3: Lower crustal magma ponding zone

We interpret this high conductivity anomaly to be caused by the presence of electrically conductive basaltic melt. Hence, C3 represents a zone of melt ponding at the base of the crust. A quantitative melt fraction estimate within the C3 is given in Section 3.2.2. The interpretation of C3 as a lower crustal melt ponding zone is supported by seismic observations, geodynamic modelling studies and petrological models for melt evolution and transport in the MER. In the following these studies are presented in more detail.

Analysis of seismic S to- P receiver functions provides evidence for a thinned lithosphere and upwelling asthenosphere below the rift valley (Rychert et al., 2012). A pronounced low seismic velocity anomaly is observed in the upwelling asthenosphere, which can only be explained by presence of melt that originates from decompression melting (e.g. Chambers et al., 2022; Kim et al., 2012; Rychert et al., 2012). It has been shown that the Moho deepens from West to East in this area (Fig. 3), indicating that asthenospheric upwelling is slightly asymmetric to the rift axis and more pronounced under the western part of the rift (e.g. Keranen & Klemperer, 2008; Stuart et al., 2006). Geodynamic modelling by (Rychert et al., 2012) shows that melt generated through decompression melting experiences strong buoyancy forces causing it to migrate into the lower crust, where it accumulates in a melt ponding zone above the Moho. The C3 structure in our model is spatially coherent with an identified low shear wave velocity anomaly, that has been interpreted as such a melt ponding reservoir (e.g. Chambers et al., 2022; Kim et al., 2012).

The observation that melt is asymmetrically distributed across the rift has also been made by a regional MT study, approximately 110 km north of our study area (Whaler & Hautot, 2006). There, authors report high electrical conductivities west of the rift-axis at a depth of about 25 km.

That the lower crustal melt emplacement and asthenospheric upwelling occur asymmetric with respect to the rift axis is not surprising. The tectonic analogue modelling has suggested that the distribution of melt in the crust is guided by en-échelon structures, such as the SDFZ and the WFB volcano-tectonic segments (Corti, 2009, and references therein). However, it is interesting that lower crustal melt ponding is restricted to the area under the SDFZ en-échelon segment, whereas no melt is ponding in the lower crust under the WFB en-échelon segment, which is a much more active region in terms of volcano-tectonic activity (e.g. Mazzarini et al., 2013). We suggest that the focusing of magma to the west is likely caused by an "inherited" structure from the early rifting stage. In general, magma emplacement during early stages of rifting could be dominated by a lateral squeezing of the melt from the rift axis towards the border faults, as demonstrated by analogue modelling

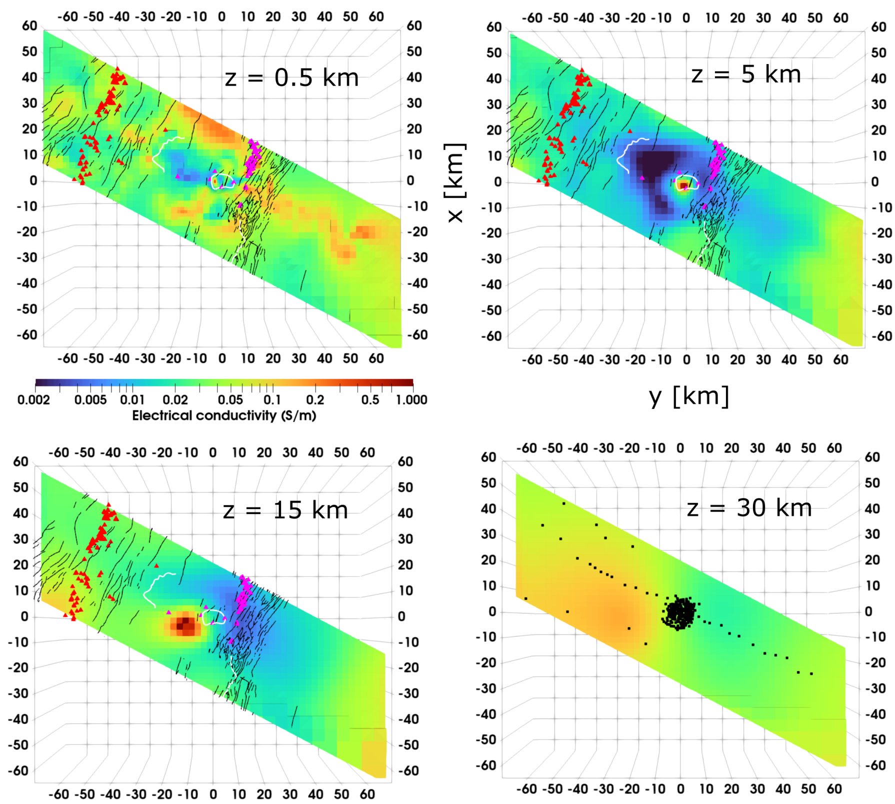

Figure 4. Horizontal slices at several depths from $z = 0.5 - 30\,\mathrm{km\,b.s.l.}$ through the final impedance tensor model. It is evident from the figure that maximum electrical conductivities occur locally confined to the WSW of Aluto. Pink and red triangles depict WFB and SDFZ vents, respectively, black lines are faults and white lines are the western Gademotta caldera rim and the proposed Aluto caldera rim. Black dots on the 30 km b.s.l. depth slice indicate MT site locations.

studies (see Fig. 29 in Corti et al., 2003). Because rift development was asymmetric (e.g. Ebinger, 2005), with master border faults at the western side (e.g. in Corti et al., 2018, Fig. 2, profile 3), it is likely that the melt was favourably squeezed towards the western border faults, ultimately leading to the presently observed western asymmetric melt distribution. Hence, the observed asymmetric melt distribution is plausible, even though major present-day volcano-tectonic structures are found to the east of the rift axis.

Further, our electrical conductivity model suggests that the melt is not distributed uniformly along the imaged en-échelon segment of the SDFZ, rather the melt is focused in a region spatially confined to the WSW of Aluto (Fig. 4, Fig. 5). To the best of our knowledge, such detailed variations of along-rift melt distributions have not been resolved

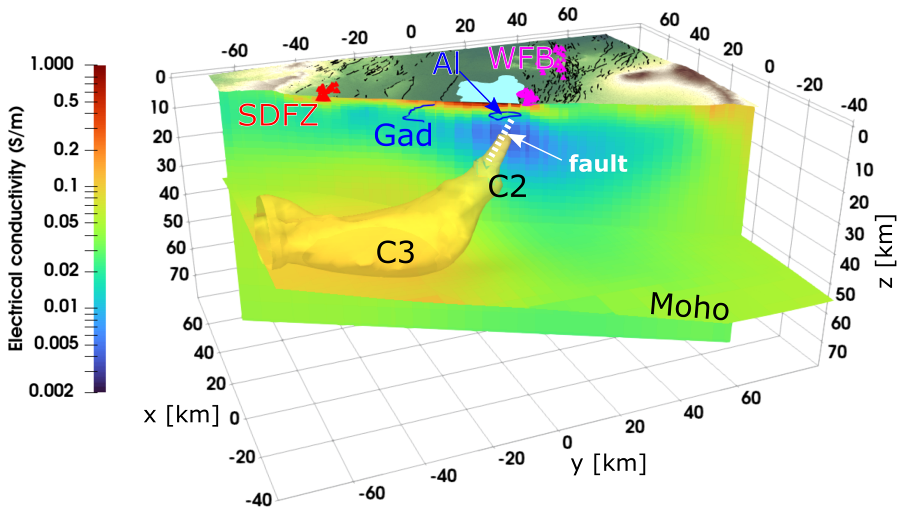

Figure 5. Vertical slice through the final model, approximately along the northern profile line of the MT sites (see Fig. 1). The Moho, as in Fig. 3, is colored by the electrical conductivities at the corresponding depth. The $\sigma = 0.1\,\mathrm{S/m}$-isosurface illustrates the extent of the magmatic ascent channel (C2) and the lower crustal melt ponding zone (C3). The magma ascent channel (C2) is situated exactly beneath Aluto and follows the dip angle of the WFB faults ($65\,^\circ$: Corti (2009)). The dipping of faults intersecting Aluto is indicated as a dashed white line. The melt ponding zone (C3) is confined to the area west of the rift-axis and WSW of Aluto volcano. Its lower bound roughly coincides with the Moho. Vents at the WFB and SDFZ are represented as red and pink triangles, respectively. The Gademotta (Gad) caldera rim is shown as a blue line, faults as black lines.

in the existing regional seismic models (e.g. Chambers et al., 2022; Kim et al., 2012). Our model indicates that lower crustal melt emplacement occurs much more punctuated and locally than previous geophysical models have shown and than tectonic analogue models have suggested (Corti, 2009, and references therein).

3.2.2 Melt fraction estimates

The model obtained from this study allows us to use electrical conductivity as an independent constraint to quantify the amount of basaltic melt present in the lower crust. Until now, such estimates in the CMER relied mainly on seismic studies, of which some are summarized in the SI (Tab. S2). Adding electrical conductivity as an additional constraint reduces uncertainty of melt estimates and adds previously lacking knowledge on the spatial extent of the melt reservoir. To estimate the melt content, we used the experiment-calibrated model by Ni et al. (2011) (SI: Text S6), which parameterizes the electrical conductivity of basaltic melt in terms of temperature and dissolved water content. The estimated temperature range for the primary basaltic melt within our interpreted source region (C3) is $\mathcal{T} = 1300 - 1400\,^{\circ}\mathrm{C}$ (SI: Tab. S2). Thermodynamic modelling of melt evolution constrains the dissolved water content within the parental basaltic melt of samples erupted at Aluto (Gleeson et al., 2017) to $c_{H2O}^{melt} <= 1\,\mathrm{wt\%}$. This amount is well below the maximum water solubility of $\max(c_{H2O}^{melt}) = 6.7\,\mathrm{wt\%}$ for identical magma storage conditions, which we calculated using MagmaSat by Ghiorso and Gualda (2015).

Under the relevant conditions (see SI: Tab. S2), the electrical conductivity of a basaltic melt is approximately $\sigma_{melt} = 2.9 - 8.4\,\mathrm{S/m}$ (SI: Fig. S15). Based on the basaltic melt conductivity and the observed range of $\sigma_{bulk} = 0.1 - 0.18\,\mathrm{S/m}$ in the magma ponding zone (C3), we calculate the melt fraction, using a modified Archie's law (SI: Eq. 17 Glover, 2015). The melt fraction is estimated for high melt-connectivities, reflected by a cementation exponent of $m = 1.15$, corresponding to the upper Hashin-Shtrikman bound, and lower connectivities, reflected by $m = 1.5$, which correspond to interstitial melt storage in a matrix of closely packed, perfect spheres (e.g. Glover, 2015). With these constraints, the melt fraction within the C3 conductor is $1.8-7.1$ vol.% and $4.5-14.7$ vol.% for maximum and minimum basaltic melt conductivities, respectively. Seismic studies estimated $2-7$ vol.% of vertically aligned melt, based on modelling seismic velocities and seismic anisotropies in the uppermost mantle (Hammond & Kendall, 2016, SI: Tab. S2), fitting well into the range of our estimates. However, given the estimates from seismic studies, our maximum estimated melt fraction of 14.7 vol.% appears rather high. Taking into account that a melt fraction of 14.7 vol.% would be even higher than what has been estimated from a MT study in the Afar region (Desissa et al., 2013, SI: Tab. S2), where rifting is far more advanced and thus higher melt fractions are expected (e.g. Keranen & Klemperer, 2008). We consider our maximum estimate of 14.7 vol.%, and the underlying connectivity model, to be unrealistic, suggesting that higher temperatures, higher water contents and better melt connectivities are the conditions that better describe the in situ setting. In this case, our maximum estimated melt fraction is 7 vol.%. These estimated melt fractions are in agreement with independent estimates that are based on seismic velocities (see SI: Tab. S2) and support the interpretation of the C3 conductor to be a lower crustal magma ponding zone.

3.2.3 C2: Transcrustal magma ascent channel

We interpret the upward rising conductor C2 to be the magma ascent channel in which melt migrates from the deeper melt ponding zone (C3) to the shallow magmatic system beneath Aluto (Fig. 4, 5). The enhanced conductivity within C2 requires that melt is present in the channel up to shallow depths of about 3 km b.s.l.. Hence, the upper part of C2 also represents the magmatic heat source of Aluto's geothermal reservoir (Fig. 3 b). The interpretation of C2 as a mature magmatic ascent channel is supported by petrological studies, which predict that magma under the WFB rises quickly towards the surface, where it either stalls and fractionates to eventually erupt as rhyolite, or the melt erupts quickly as basalt (Mazzarini et al., 2013; Rooney et al., 2011). Another evidence for melt fractions within C2 beneath Aluto is the observed aseismic zone in roughly the same area that was interpreted as hot ductile crust (Wilks et al., 2020). The shallower part of channel C2 has already been described by Samrock et al. (2020, 2021), who noted that the dip of the channel ($\sim 65\,^{\circ}$) is coherent with the dominant fault plane of faults intersecting Aluto volcano. A strong link between magmatic pathways and tectonically weak zones has been described by numerous studies investigating magma-assisted continental rifting (e.g. Casey et al., 2006). The close coupling between active tectonic structures and magma pathways in the central MER is directly observable from the distribution of vents (Fig. 1), which shows that magma preferentially rises along fault zones, where the crust has been weakened (e.g. Mazzarini et al., 2013). The spatial conjunction of tectonic and magmatic features furthermore supports the concept of "self-sustained" magmatic segments, where strain is preferentially localized in magmatic segments, which promote intrusions (Beutel et al., 2010).

3.2.4 R1: Solidified igneous rock

The most striking feature of this electrical resistor is that it is clearly bounded to the west by the Gademotta caldera rim (Fig. 4). The spatial correlation between R1 and the Caldera rim leads us to the most plausible interpretation that R1 constitutes cooled intrusive rock, as has already been previously suggested (Hübert et al., 2018; Samrock et al., 2020). Its formation is likely related to the formation of the Gademotta caldera, where volcanism ceased 1 Ma ago (Hutchison et al., 2016b).

3.2.5 C1: Aquifer/sediment unit

In agreement with the conceptual hydrogeological model of the study area by Ghiglieri et al. (2020), the conductor C1 images a shallow layer of pyroclastics and lavas that has been classified as a fissured aquifer. Considering reported groundwater electrical conductivities in the area (Burnside et al., 2021), the most widely distributed observed bulk conductivities within C1 ($\sigma = 0.1 - 0.2\,\mathrm{S/m}$) would require an unreasonably large fluid fraction within C1 (see SI: Text S6.2). It is thus likely that enhanced conductivities in C1 are attributed to a superposition of ionic conduction in porous rocks and sediments as well as electrical conduction through conductive compounds such as clays, which also form through rock weathering processes and are commonly found in soils around the study area (Fritzsche et al., 2007).

3.2.6 Geothermal system

The shallow cap-like conductor ($\sigma = 0.1 - 0.3\,\mathrm{S/m}$), shown in Fig. 3 b under Aluto volcano down to depths of 1.5 km below surface, and the underlying zone of decreased electrical conductivities ($\sigma = 0.02\,\mathrm{S/m}$) between the cap and the upper part of the magma ascent channel C2 are typical features of volcano-hosted, high-temperature geothermal systems. The electrically conductive cap represents the argillic alteration zone, where electrically conductive clays are formed along the flow paths of circulating hot fluids on top of the convective hydrothermal reservoir, at temperatures of $\mathcal{T} \approx 80 - 180\,^{\circ}\mathrm{C}$ (e.g. Kristmannsdottir, 1979; Lévy et al., 2018). An electrically more resistive region under the clay cap represents the propylitic alteration zone, where less electrically conductive alteration minerals form at higher temperatures of $\mathcal{T} > 250\,^{\circ}\mathrm{C}$. The C2 structure is the heat source that drives hydrothermal convection (Fig. 3 b). A more detailed description of the geothermal system can be found in previous local MT studies of the Aluto-Langano geothermal field (Cherkose & Mizunaga, 2018; Samrock et al., 2015, 2020).

3.3 Discussion

The electrical conductivity structure, revealed by our 3-D multi-scale model, is in agreement with the concept and models of magma-assisted continental rifting. A unique feature of our new 3-D model is that it images both the distribution of melt throughout the crust and the geothermal system. Based on this model and previous studies, we present an updated conceptual model of the central MER in Fig. 6.

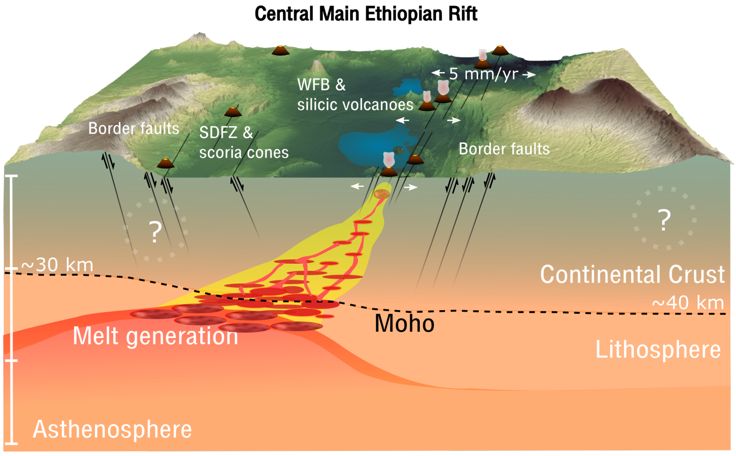

Figure 6. Conceptual model of the CMER. Asthenospheric upwelling leads to decompression melting. Buoyancy effects lead to upward migration of melt and melt ponding in the lower crust. Magma from the lower crustal ponding zone is fed into transcrustal magmatic mush systems that form along structural damage zones. A major part of the crustal extension ($\sim 5\,\mathrm{mm/yr}$) occurs in the WFB (e.g. Bilham et al., 1999). The transcrustal magmatic system below the WFB is well developed. Here, magma rises quickly and fractionates in shallow magma reservoirs beneath silicic volcanoes, such as Aluto. The transcrustal magmatic system below the SDFZ is less mature and is not clearly imaged in this study. This might be caused by a lack of significant amounts of electrically conductive melt below the SDFZ, combined with a sparser MT site spacing in this area. Areas in the conceptual model that are less constrained by data are indicated by a question mark.

In general, magmatic underplating and ponding in stacked sills at the base of the crust, as is seen in our model (C3), is a widely adopted concept, but detailed imaging of such zones is rare (e.g. Cashman et al., 2017; Thybo & Artemieva, 2013). Analogue modelling has demonstrated that continental rifting undergoes an evolution during which magma first accumulates below border faults of the rift valley and is later focused towards en-échelon tectono-magmatic segments in the rift center (see Fig. 29 in Corti et al., 2003). Our model suggests that both stages of this evolution are still happening and influence the rift architecture, as the lower crustal ponding zone (C3) is asymmetric to the rift valley, close to western border faults, and as the magma ascent channel (C2) below the WFB follows the dip angle of the eastern border and the WFB faults.

Furthermore, the presented multi-scale model reconciles the concept of transcrustal magmatic mush systems, where magma storage happens at multiple interconnected levels in the crust, rather than in isolated voluminous magma chambers (e.g. Cashman et al., 2017). Indeed, in our model, magma accumulates in the lower crust (C3), where high temperatures maintain melt-bearing regions, even if the magma concentration is low. Segregated magma migrates upwards along zones of crustal weaknesses to shallower crustal levels (C2), where melt is stored in a smaller upper crustal reservoir (Fig. 3 b), which represents only the small, uppermost part of a much larger magmatic system (Cashman et al., 2017). Hence the WFB and the magma ascent channel (C2) form a well-developed tectono-magmatic system that allows melt to rise quickly (e.g. Mazzarini et al., 2013; Rooney et al., 2011). In contrast to the crustal structure below the WFB, our model does not show enhanced upper crustal conductivities below the monogenetic vents in the western SDFZ region (Figs. 3,5). Such anomalies could have been expected since C3 is the most obvious source of magma for magmatic vents in the SDFZ. The absence of a significant electrical conductivity anomaly under the SDFZ can be explained by the fact that ancient magma channels of the monogenetic vents are ephemeral and cooled quickly. If small amounts of melt are still present, melt is probably stored in form of a highly crystalline and poorly interconnected mush and is therefore more difficult to image, given the rather sparse distribution of MT stations in this region. This is supported by petrologial studies, which suggest that melt rises in a complex dike system and is stored at multiple levels under the the SDFZ, where it cools (e.g. Mazzarini et al., 2013; Rooney et al., 2011). The absence of significant amounts of melt in the upper crust under SDFZ is also in agreement with the observed low seismic activity beneath this area (Keir et al., 2006), which hints at much fewer or no ongoing intrusions in that region. However, we note again that the $5 - 10$ km site spacing in that area is much larger than at Aluto and smaller-scale variations under the SDFZ might remain undetected in our model. Despite the absence of significant conductivity anomalies in the upper crust under the SDFZ, it is important to point out that volcanic activity in the SDFZ most likely originates from the imaged deeper magmatic ponding zone (C3). Thus, our model suggests that magmas, erupted at the SDFZ and at Aluto within the WFB, may come from a common magma source, which would be the lower crustal magma ponding zone (C3) in our nomenclature. Although some geochemical studies have suggested spatially separated lower crustal melt ponding zones for the volcanoes located along the fault zones of the SDFZ and the WFB (e.g. Rooney et al., 2011), recent studies show that compositional variations can be explained solely by different rates of magma ascent rather than by the existence of distinct melt reservoirs (Nicotra et al., 2021).

Our current 3-D model differs in parts from the 2-D model by Hübert et al. (2018), who performed a 2-D inversion of the 120 km long MT profile crossing Aluto (Fig. 1, see SI: Tab. 1). (Hübert et al., 2018) imaged a strong conductivity anomaly below the SDFZ, situated at much shallower depths than the lower magma ponding zone (C3) in our model. Furthermore, the 2-D model of (Hübert et al., 2018) did not image a magma ascent channel between the deeper source and the Aluto volcano. There can be several reasons for the observed differences between the models. First, a large portion of the data exhibit 3-D effects (see SI: Fig. S5) and, indeed, we observe significant conductivity variations along the rift (Fig. 4), which demand and justify a 3-D modelling approach. Additionally, the density of MT sites in our new study is significantly higher around Aluto, which can further contribute to the observed differences.

4 Conclusions and Outlook

Our model provides a 3-D subsurface image of the Aluto volcano region in the MER and reveals regional geological structures across the rift and a local geothermal system under Aluto. The main contributions of this study concern the understanding of the magma-assisted rifting of the MER and its geothermal systems, namely: (i) imaging the lower crustal magmatic ponding zone with MT and thereby adding another geophysical constraint (electrical conductivity) to its characterization and (ii) imaging, for the first time, the entire volcano-hydrothermal system under Aluto, along with its connection to the deep-seated lower crustal magma source.

The number of geophysical models imaging transcrustal magmatic mush systems at this scale (e.g. Cashman et al., 2017) is still limited (e.g. Comeau et al., 2015; Hill et al., 2022; Huang et al., 2015), especially when the setting of actively evolving continental rifts is considered. Our detailed study provides previously missing geophysical evidence for the hypothesized (e.g. Ebinger, 2005; Rooney et al., 2011) conceptual model of the CMER (Fig. 6).

These observations, and the subsequent geological interpretation, were enabled by combining regional and local MT datasets and by using a modern multi-scale magnetotelluric imaging approach. Future regional-scale MT studies along the rift valley are required to provide further insights into along-rift variations of the lower crustal magma ponding zone (C3) and its connection to the volcanic geothermal centers of Tulu Moye and Corbetti, where high-resolution MT surveys, comparable to Aluto, have been conducted (Gíslason et al., 2015; Samrock et al., 2018).

Data availability

The MT data collected at Aluto by ETH Zurich are available from Samrock et al. (2010) via the IRIS EMTF Database: `http://ds.iris.edu/spud/emtf` under the Project entry "Ethiopia", and the survey name "Aluto-Langano Geothermal" . The MT-dataset by project RiftVolc is available from Hübert and Whaler (2020) by DOI: `10.5285/2fb02ed4-5f50-4c14-aeec-27ee13aafc38`. The MT data by the Geological Survey of Ethiopia are available for academic purposes on request from the Geological Survey of Ethiopia, as was the case for this study. The model will be made available for download in the ETH research collection (`www.research-collection.ethz.ch`) under Dambly et al. (2022) (DOI: `10.3929/ethz-b-000576313`) in form of a Visualization Toolkit (VTK) data file for ParaView.

Declaration of competing interest

The authors declare that they have no known competing financial interests or personal relationships that could have appeared to influence the work reported in this paper.

CReDit Authorship statement

M.L.T.D. performed modelling and inversion of the magnetotelluric data, model visualization and developed numerical tools. F.S. contributed to the 3-D modelling and inversion of the data and model visualization. A.G. developed the GoFEM code and contributed to the 3-D modelling and inversion of the data. All authors interpreted the results and contributed to the writing and review of the paper.

Acknowledgments

M.L.T.D. was supported by ETH Grant ETH-02 19-1. A.G. was supported by the Heisenberg Grant from the German Research Foundation, Deutsche Forschungsgemeinschaft (Project No. 465486300). 3-D inversions and modelling were carried out at the Swiss National Supercomputing Center (CSCS) under project ID s1106. We thank Juliane Hübert and Kathy Whaler from Project RiftVolc and the Geological Survey of Ethiopia for making MT data available. We acknowledge the use of MTPy (Kirkby et al., 2019; Krieger & Peacock, 2014), Generic Mapping Tools (GMT), and Paraview, and thank NASA for providing SRTM digital elevation models. M.O.S., F.S. and M.L.T.D. thank the Werner Siemens

Foundation (Werner Siemens-Stiftung) for their endowment of the Geothermal Energy and Geofluids (GEG.ethz.ch) group at ETH Zurich.

References

Agostini, A., Bonini, M., Corti, G., Sani, F., & Manetti, P. (2011a). Distribution of quaternary deformation in the central Main Ethiopian Rift, East Africa. *Tectonics*, *30*(4), 1–21. doi: 10.1029/2010TC002833

Agostini, A., Bonini, M., Corti, G., Sani, F., & Manetti, P. (2011b). *Distribution of quaternary deformation in the central Main Ethiopian Rift, East Africa* [dataset]. (Access Fault Dataset 2.5 `http://ethiopianrift.igg.cnr.it/utilities.htm`) doi: 10.1029/2010TC002833

Arndt, D., Bangerth, W., Blais, B., Clevenger, T. C., Fehling, M., Grayver, A. V., … Wells, D. (2020). The deal. II library, version 9.2. *Journal of Numerical Mathematics*, *28*(3), 131–146. doi: 10.1515/jnma-2020-0043

Beutel, E., van Wijk, J., Ebinger, C., Keir, D., & Agostini, A. (2010). Formation and stability of magmatic segments in the Main Ethiopian and Afar Rifts. *Earth and Planetary Science Letters*, *293*(3-4), 225–235. doi: 10.1016/j.epsl.2010.02.006

Biggs, J., Ayele, A., Fischer, T. P., Fontijn, K., Hutchison, W., Kazimoto, E., … Wright, T. J. (2021). Volcanic activity and hazard in the East African Rift zone. *Nature Communications*, *12*(1), 1–12. doi: 10.1038/s41467-021-27166-y

Bilham, R., Bendick, R., Larson, K., Mohr, P., Braun, J., Tesfaye, S., & Asfaw, L. (1999). Secular and tidal strain across the Main Ethiopian Rift. *Geophysical Research Letters*, *26*(18), 2789–2792. doi: 10.1029/1998GL005315

Bonini, M., Corti, G., Innocenti, F., Manetti, P., Mazzarini, F., Abebe, T., & Pecskay, Z. (2005, February). Evolution of the Main Ethiopian Rift in the frame of Afar and Kenya rifts propagation. *Tectonics*, *24*(1). doi: 10.1029/2004TC001680

Burnside, N., Montcoudiol, N., Becker, K., & Lewi, E. (2021). Geothermal energy resources in Ethiopia: Status review and insights from hydrochemistry of surface and groundwaters. *Wiley Interdisciplinary Reviews: Water*, e1554. doi: 10.1002/wat2.1554

Cagniard, L. (1953, July). Basic theory of the magneto-telluric method of geophysical prospecting. *Geophysics*, *18*(3), 605–635. doi: 10.1190/1.1437915

Caldwell, T. G., Bibby, H. M., & Brown, C. (2004). The magnetotelluric phase tensor. *Geophysical Journal International*, *158*(2), 457–469. doi: 10.1111/j.1365-246X.2004

.02281.x

capitalethiopia.com. (2022). *Production tests kick start at Aluto Langano.* Retrieved from `https://www.capitalethiopia.com/capital/production-tests-kick-start-at-aluto-langano/` (accessed 14 October 2022)

Casey, M., Ebinger, C. J., Keir, D., Gloaguen, R., & Mohamed, F. (2006). Strain accommodation in transitional rifts: Extension by magma intrusion and faulting in Ethiopian rift magmatic segments. *Environmental Geochemistry and Health, With Special Reference to Developing Countries*, *259*(2003), 143–163. doi: 10.1144/GSL.SP.2006.259.01.13

Cashman, K. V., Sparks, R. S. J., & Blundy, J. D. (2017). Vertically extensive and unstable magmatic systems: A unified view of igneous processes. *Science*, *355*(6331). doi: 10.1126/science.aag3055

Chambers, E. L., Harmon, N., Rychert, C. A., Gallacher, R. J., & Keir, D. (2022, 04). Imaging the seismic velocity structure of the crust and upper mantle in the northern East African Rift using rayleigh wave tomography. *Geophysical Journal International*. doi: 10.1093/gji/ggac156

Cherkose, B. A., & Mizunaga, H. (2018). Resistivity imaging of Aluto-Langano geothermal field using 3-D magnetotelluric inversion. *Journal of African Earth Sciences*, *139*, 307-318. doi: 10.1016/j.jafrearsci.2017.12.017

Comeau, M. J., Unsworth, M. J., Ticona, F., & Sunagua, M. (2015). Magnetotelluric images of magma distribution beneath Volcán Uturuncu, Bolivia: Implications for magma dynamics. *Geology*, *43*(3), 243–246. doi: 10.1130/G36258.1

Corti, G. (2009). Continental rift evolution: From rift initiation to incipient break-up in the Main Ethiopian Rift, East Africa. *Earth-Science Reviews*, *96*(1-2), 1–53. doi: 10.1016/j.earscirev.2009.06.005

Corti, G., Bonini, M., Conticelli, S., Innocenti, F., Manetti, P., & Sokoutis, D. (2003). Analogue modelling of continental extension: A review focused on the relations between the patterns of deformation and the presence of magma. *Earth-Science Reviews*, *63*(3-4), 169–247. doi: 10.1016/S0012-8252(03)00035-7

Corti, G., Sani, F., Agostini, S., Philippon, M., Sokoutis, D., & Willingshofer, E. (2018). Off-axis volcano-tectonic activity during continental rifting: Insights from the transversal Goba-Bonga lineament, Main Ethiopian Rift (East Africa). *Tectonophysics*, *728-729*, 75–91. doi: 10.1016/j.tecto.2018.02.011

Dambly, M. L. T., Samrock, F., Grayver, A., & Saar, M. O. (2022). *Transcrustal 3-D electrical conductivity model of the Central Main Ethiopian Rift* [Model]. doi: 10.3929/ethz-b-000576313

Desissa, M., Johnson, N. E., Whaler, K. A., Hautot, S., Fisseha, S., & Dawes, G. J. (2013). A mantle magma reservoir beneath an incipient mid-ocean ridge in Afar, Ethiopia. *Nature Geoscience*, *6*(10), 861–865. doi: 10.1038/ngeo1925

Ebinger, C. (2005, 04). Continental break-up: The East African perspective. *Astronomy & Geophysics*, *46*(2), 2.16-2.21. doi: 10.1111/j.1468-4004.2005.46216.x

Fontijn, K., McNamara, K., Tadesse, A. Z., Pyle, D. M., Dessalegn, F., Hutchison, W., ... Yirgu, G. (2018). Contrasting styles of post-caldera volcanism along the Main Ethiopian Rift: Implications for contemporary volcanic hazards. *Journal of Volcanology and Geothermal Research*, *356*, 90–113. doi: 10.1016/j.jvolgeores.2018.02.001

Fritzsche, F., Zech, W., & Guggenberger, G. (2007). Soils of the Main Ethiopian Rift valley escarpment: A transect study. *CATENA*, *70*(2), 209-219. doi: 10.1016/j.catena.2006.09.005

Gallacher, R. J., Keir, D., Harmon, N., Stuart, G., Leroy, S., Hammond, J. O., ... Ahmed, A. (2016). The initiation of segmented buoyancy-driven melting during continental breakup. *Nature Communications*, *7*, 1–9. doi: 10.1038/ncomms13110

Ghiglieri, G., Pistis, M., Abebe, B., Azagegn, T., Asresahagne Engidasew, T., Pittalis, D., ... Haile, T. (2020). Three-dimensional hydrostratigraphical modelling supporting the evaluation of fluoride enrichment in groundwater: Lakes basin (Central Ethiopia). *Journal of Hydrology: Regional Studies*, *32*, 100756. doi: 10.1016/j.ejrh.2020.100756

Ghiorso, M. S., & Gualda, G. A. (2015). An H_2O–CO_2 mixed fluid saturation model compatible with rhyolite-MELTS. *Contributions to Mineralogy and Petrology*, *169*(6), 1–30. doi: 10.1007/s00410-015-1141-8

Gíslason, G., Eysteinsson, H., Björnsson, G., & Hardardóttir, V. (2015). Results of surface exploration in the Corbetti geothermal area, Ethiopia. In *Proceedings world geothermal congress.* Melbourne, Australia.

Gleeson, M. L., Stock, M. J., Pyle, D. M., Mather, T. A., Hutchison, W., Yirgu, G., & Wade, J. (2017). Constraining magma storage conditions at a restless volcano in the Main Ethiopian Rift using phase equilibria models. *Journal of Volcanology and Geothermal Research*, *337*, 44–61. doi: 10.1016/j.jvolgeores.2017.02.026

Glover, P. (2015, April). Geophysical properties of the near surface Earth: Electrical properties. In G. Schubert (Ed.), *Treatise on geophysics* (Second ed., pp. 89–137). Elsevier Oxford. doi: 10.1016/B978-0-444-53802-4.00189-5

Grayver, A. V. (2015). Parallel three-dimensional magnetotelluric inversion using adaptive finite-element method. part i: Theory and synthetic study. *Geophysical Journal International*, *202*(1), 584–603. doi: 10.1093/gji/ggv165

Grayver, A. V., & Kolev, T. V. (2015). Large-scale 3D geoelectromagnetic modeling using parallel adaptive high-order finite element method. *Geophysics*, *80*(6), E277–E291. doi: 10.1190/geo2015-0013.1

Hammond, J. O., & Kendall, J. M. (2016). Constraints on melt distribution from seismology: A case study in Ethiopia. *Environmental Geochemistry and Health, With Special Reference to Developing Countries*, *420*(1), 127–147. doi: 10.1144/SP420.14

Hill, G. J., Wannamaker, P. E., Maris, V., Stodt, J. A., Kordy, M., Unsworth, M. J., ... Kyle, P. (2022). Trans-crustal structural control of CO_2-rich extensional magmatic systems revealed at Mount Erebus Antarctica. *Nature Communications*, *13*(1), 1–10. doi: 10.1038/s41467-022-30627-7

Huang, H.-H., Lin, F.-C., Schmandt, B., Farrell, J., Smith, R. B., & Tsai, V. C. (2015). The Yellowstone magmatic system from the mantle plume to the upper crust. *Science*, *348*(6236), 773–776. doi: 10.1126/science.aaa5648

Hübert, J., & Whaler, K. (2020). *Magnetotelluric and transient electromagnetic data from the Main Ethiopian Rift. British Geological Survey. (dataset).* [dataset]. doi: 10.5285/2fb02ed4-5f50-4c14-aeec-27ee13aafc38

Hübert, J., Whaler, K., & Fisseha, S. (2018). The electrical structure of the central Main Ethiopian Rift as imaged by magnetotellurics: Implications for magma storage and pathways. *Journal of Geophysical Research, Solid Earth*, *123*(7), 6019–6032. doi: 10.1029/2017JB015160

Hutchison, W., Biggs, J., Mather, T. A., Pyle, D. M., Lewi, E., Yirgu, G., ... Fischer, T. P. (2016b). Causes of unrest at silicic calderas in the East African Rift: New constraints from InSAR and soil-gas chemistry at Aluto volcano, Ethiopia. *Geochemistry, Geophysics, Geosystems*, *17*(8), 3008–3030. doi: 10.1002/2016GC006395

Iddon, F., & Edmonds, M. (2020). Volatile-rich magmas distributed through the upper crust in the Main Ethiopian Rift. *Geochemistry, Geophysics, Geosystems*, *21*(6). doi: 10.1029/2019GC008904

IRENA. (2020). *Geothermal development in Eastern Africa: Recommendations for power* *and direct use*. Abu Dhabi: International Renewable Energy Agency.

Jolie, E., Scott, S., Faulds, J., Chambefort, I., Axelsson, G., Gutiérrez-Negrín, L. C., … Zemedkun, M. T. (2021). Geological controls on geothermal resources for power generation. *Nature Reviews Earth & Environment*, *2*(5), 324–339. doi: 10.1038/s43017-021-00154-y

Käufl, J. S., Grayver, A. V., Comeau, M. J., Kuvshinov, A. V., Becken, M., Kamm, J., … Demberel, S. (2020). Magnetotelluric multiscale 3-D inversion reveals crustal and upper mantle structure beneath the Hangai and Gobi-Altai region in Mongolia. *Geophysical Journal International*, *221*(2), 1002–1028. doi: 10.1093/gji/ggaa039

Käufl, J. S., Grayver, A. V., & Kuvshinov, A. V. (2018). Topographic distortions of magnetotelluric transfer functions: A high-resolution 3-D modelling study using real elevation data. *Geophysical Journal International*, *215*(3), 1943–1961. doi: 10.1093/gji/ggy375

Kebede, S., Fikru, W., & Tesfaye, K. (2020). Status of geothermal exploration and development in Ethiopia. In *Proceedings world geothermal congress.*

Keir, D., Ebinger, C. J., Stuart, G. W., Daly, E., & Ayele, A. (2006). Strain accommodation by magmatism and faulting as rifting proceeds to breakup: Seismicity of the northern Ethiopian Rift. *Journal of Geophysical Research, Solid Earth*, *111*(5), 1–17. doi: 10.1029/2005JB003748

Kendall, J.-M., & Lithgow-Bertelloni, C. (2016). Why is Africa rifting? *Environmental Geochemistry and Health, With Special Reference to Developing Countries*, *420*(1), 11–30. doi: 10.1144/SP420.17

Kendall, J.-M., Stuart, G., Ebinger, C., Bastow, I., & Keir, D. (2005, January). Magma-assisted rifting in Ethiopia. *Nature*, *433*(7022), 146–148. doi: 10.1038/nature03161

Keranen, K., & Klemperer, S. L. (2008). Discontinuous and diachronous evolution of the Main Ethiopian Rift: Implications for development of continental rifts. *Earth and Planetary Science Letters*, *265*(1-2), 96–111. doi: 10.1016/j.epsl.2007.09.038

Kim, S., Nyblade, A. A., Rhie, J., Baag, C. E., & Kang, T. S. (2012). Crustal S-wave velocity structure of the Main Ethiopian Rift from ambient noise tomography. *Geophysical Journal International*, *191*(2), 865–878. doi: 10.1111/j.1365-246X.2012.05664.x

King, G., & Bailey, G. (2006). Tectonics and human evolution. *Antiquity*, *80*(308), 265–286. doi: 10.1017/S0003598X00093613

Kirkby, A. L., Zhang, F., Peacock, J., Hassan, R., & Duan, J. (2019). The MTPy software package for magnetotelluric data analysis and visualisation. *Journal of Open Source Software*, *4*(37), 1358. doi: 10.21105/joss.01358

Krieger, L., & Peacock, J. R. (2014). MTpy: A python toolbox for magnetotellurics. *Computers & Geosciences*, *72*, 167-175. doi: 10.1016/j.cageo.2014.07.013

Kristmannsdottir, H. (1979). Alteration of basaltic rocks by hydrothermal-activity at 100-300°C. In M. Mortland & V. Farmer (Eds.), *International clay conference 1978* (Vol. 27, p. 359-367). Elsevier. doi: 10.1016/S0070-4571(08)70732-5

Lévy, L., Gibert, B., Sigmundsson, F., Flóvenz, O. G., Hersir, G. P., Briole, P., & Pezard, P. A. (2018). The role of smectites in the electrical conductivity of active hydrothermal systems: Electrical properties of core samples from Krafla volcano, Iceland. *Geophysical Journal International*, *215*(3), 1558–1582. doi: 10.1093/gji/ggy342

Mazzarini, F., & Isola, I. (2010). Monogenetic vent self-similar clustering in extending continental crust: Examples from the East African Rift system. *Geosphere*, *6*(5), 567–582. doi: 10.1130/GES00569.1

Mazzarini, F., Rooney, T. O., & Isola, I. (2013). The intimate relationship between strain and magmatism: A numerical treatment of clustered monogenetic fields in the Main Ethiopian Rift. *Tectonics*, *32*(1), 49–64. doi: 10.1029/2012TC003146

Ni, H., Keppler, H., & Behrens, H. (2011). Electrical conductivity of hydrous basaltic melts: Implications for partial melting in the upper mantle. *Contributions to Mineralogy and Petrology*, *162*(3), 637–650. doi: 10.1007/s00410-011-0617-4

Nicotra, E., Viccaro, M., Donato, P., Acocella, V., & De Rosa, R. (2021). Catching the Main Ethiopian Rift evolving towards plate divergence. *Scientific Reports*, *11*(1), 1–16. doi: 10.1038/s41598-021-01259-6

Rooney, T. O., Bastow, I. D., & Keir, D. (2011). Insights into extensional processes during magma assisted rifting: Evidence from aligned scoria cones. *Journal of Volcanology and Geothermal Research*, *201*(1-4), 83–96. doi: 10.1016/j.jvolgeores.2010.07.019

Rung-Arunwan, T., Siripunvaraporn, W., & Utada, H. (2016). On the Berdichevsky average. *Physics of the Earth and Planetary Interiors*, *253*, 1–4. doi: 10.1016/j.pepi.2016.01.006

Rychert, C. A., Hammond, J. O., Harmon, N., Michael Kendall, J., Keir, D., Ebinger, C., ... Stuart, G. (2012). Volcanism in the Afar Rift sustained by decompression melting with minimal plume influence. *Nature Geoscience*, *5*(6), 406–409. doi: 10.1038/ngeo1455

Samrock, F., Grayver, A. V., Bachmann, O., Karakas, Ö., & Saar, M. O. (2021). Integrated magnetotelluric and petrological analysis of felsic magma reservoirs: Insights from Ethiopian rift volcanoes. *Earth and Planetary Science Letters*, *559*, 116765. doi: 10.1016/j.epsl.2021.116765

Samrock, F., Grayver, A. V., Cherkose, B., Kuvshinov, A., & Saar, M. O. (2020, October). Aluto-Langano geothermal field, Ethiopia: Complete image of underlying magmatic-hydrothermal system revealed by revised interpretation of magnetotelluric data. In *Proceedings world geothermal congress (wgc 2020+1)* (p. 11054). Reykjavic, Iceland. doi: 10.3929/ethz-b-000409980

Samrock, F., Grayver, A. V., Eysteinsson, H., & Saar, M. O. (2018). Magnetotelluric image of transcrustal magmatic system beneath the Tulu Moye geothermal prospect in the Ethiopian Rift. *Geophysical Research Letters*, *45*(23), 12–847. doi: 10.1029/2018GL080333

Samrock, F., Kuvshinov, A., Bakker, J., Jackson, A., & Fisseha, S. (2015). 3-D analysis and interpretation of magnetotelluric data from the Aluto-Langano geothermal field, Ethiopia. *Geophysical Journal International*, *202*(3), 1923–1948. doi: 10.1093/gji/ggv270

Samrock, F., Kuvshinov, A., Bakker, J., Jackson, A., Fisseha, S., staff of Addis Ababa University, & the Geological Survey of Ethiopia. (2010). *Magnetotelluric and vertical magnetic transfer functions acquired at the Aluto-Langano geothermal field, Ethiopia* [dataset]. (from the IRIS database, `http://ds.iris.edu/spud/emtf`) doi: 10.17611/DP/EMTF/ETHIOPIA/ETHZ

Stuart, G., Bastow, I., & Ebinger, C. (2006). Crustal structure of the northern main ethiopian rift from receiver function studies. *Geological Society, London, Special Publications*, *259*(1), 253-267. doi: 10.1144/GSL.SP.2006.259.01.20

Thybo, H., & Artemieva, I. (2013). Moho and magmatic underplating in continental lithosphere. *Tectonophysics*, *609*, 605–619. doi: 10.1016/j.tecto.2013.05.032

Tietze, K., Ritter, O., & Egbert, G. D. (2015). 3-d joint inversion of the magnetotelluric phase tensor and vertical magnetic transfer functions. *Geophysical Journal International*, *203*(2), 1128–1148. doi: 10.1093/gji/ggv347

Whaler, K., & Hautot, S. (2006). The electrical resistivity structure of the crust beneath the northern Main Ethiopian Rift. *Geological Society, London, Special Publications*, *259*(1), 293–305. doi: 10.1144/GSL.SP.2006.259.01.22

Wilks, M., Rawlinson, N., Kendall, J. M., Nowacki, A., Biggs, J., Ayele, A., & Wookey,

J. (2020). The coupled magmatic and hydrothermal systems of the restless Aluto Caldera, Ethiopia. *Frontiers in Earth Science*, *8*(October), 1–14. doi: 10.3389/feart.2020.579699

JGR: Solid Earth

Supporting Information for

The interplay of rifting, magmatism and formation of geothermal resources in the Ethiopian Rift constrained by 3-D magnetotelluric imaging

DOI:

M.L.T. Dambly[1], F. Samrock[1], A.V. Grayver[2,3], and M.O. Saar[1,4]

[1] Geothermal Energy and Geofluids group, Institute of Geophysics, ETH Zurich, Switzerland
[2] Earth and Planetary Magnetism group, Institute of Geophysics, ETH Zurich, Switzerland
[3] Institute of Geophysics and Meteorology, University of Cologne, Germany
[4] Department of Earth and Environmental Sciences, University of Minnesota, USA

Corresponding author: M.L.T. Dambly, Institute of Geophysics, ETH Zurich, Sonneggstrasse 5, 8092 Zurich, Switzerland (mdambly@ethz.ch)

Contents of this file

- Text S1 to S6
- Figures S1 to S16
- Table S1 to S2
- Movie S1

Introduction The supplementary information includes basic equations explaining the MT method (Text S1.); information on the MT dataset and how apparent resistivities of the starting model were obtained from SSQ-impedances (Text S2.); details on the mesh used for inversion and forward modelling (Text S3.); a comparison of the best fitting phase tensor and impedance tensor models (Text S4.1); an in-depth analysis of the data fit for the final impedance and phase tensor model (Text S4.2. and S4.3.); and details about the melt fraction estimation in the lower crustal magma ponding zone (Text S5.1.) and of electrical conductivities in the shallow aquifer/sediment unit (C1) (Text S5.2.).

Text S1. In the magnetotelluric (MT) method, the natural variations of the electric and magnetic field are measured on the Earth's surface. In the frequency domain, the magnetic field ($\mathbf{H}$) can be linearly related to the electric field ($\mathbf{E}$) through a transfer function, known as impedance tensor ($\mathbf{Z}$):

$$\begin{pmatrix} E_x(\mathbf{r},\omega) \\ E_y(\mathbf{r},\omega) \end{pmatrix} = \begin{pmatrix} Z_{xx}(\mathbf{r},\omega) & Z_{xy}(\mathbf{r},\omega) \\ Z_{yx}(\mathbf{r},\omega) & Z_{yy}(\mathbf{r},\omega) \end{pmatrix} \begin{pmatrix} H_x(\mathbf{r},\omega) \\ H_y(\mathbf{r},\omega) \end{pmatrix}. \tag{1}$$

Here E_i and H_i $(i \in [x,y])$ are the North (X) and East (Y) components of electric and magnetic field variations. $\mathbf{Z}$ depends on the angular frequency $\omega = 2\pi f$ and the position vector $(\mathbf{r})$. Although omitted from equation above, but all quantities also depend on distribution of the subsurface electrical conductivity $\sigma(\mathbf{r})$. Note that the reciprocal of electrical conductivity, resistivity ($\rho = 1/\sigma$), is often used interchangeably.

The complex-valued tensor elements Z_{ij} are commonly plotted in terms of their phase

$$\phi_{ij} = \tan^{-1}\left(\frac{\mathrm{Im}(Z_{ij})}{\mathrm{Re}(Z_{ij})}\right), \quad i,j \in [x,y]. \tag{2}$$

and apparent resistivity

$$\rho_{a,ij} = \frac{|Z_{ij}|^2}{\omega \mu_0}, \quad i,j \in [x,y], \tag{3}$$

where μ_0 is the magnetic permeability of free space $\mu_0 = 4\pi * 10^{-7}\,\mathrm{Vs/Am}$.

Information about the dimensionality and directionality of the conductivity structures can be obtained from the phase tensor ($\mathbf{\Phi}$) (e.g. *Caldwell et al.*, 2004):

$$\mathbf{Z} = \mathrm{Re}(\mathbf{Z}) + \mathrm{Im}(\mathbf{Z}) = X + iY, \quad \mathbf{\Phi} = X^{-1}Y \tag{4}$$

The phase tensor $\mathbf{\Phi}$ can be visualized as an ellipse, that is mathematically described by one direction (α) and three rotational invariants ($\beta, \Phi_{min}, \Phi_{max}$), where $\mathbf{R}$ is the rotation matrix:

$$\mathbf{\Phi} = \mathbf{R}^T(\alpha - \beta) \begin{pmatrix} \Phi_{max} & 0 \\ 0 & \Phi_{min} \end{pmatrix} \mathbf{R}(\alpha + \beta) \tag{5}$$

The tilt angle ($\alpha - \beta$) of the $\mathbf{\Phi}$-ellipse represents the electric strike direction at the measurement location for the respective sounding period. In case of a 2-D subsurface Φ_{min} and Φ_{max} will be parallel and perpendicular to the linearly polarized $\mathbf{E}$- and $\mathbf{H}$-fields.

Text S2. The magnetotelluric dataset of our study is a combination of different surveys conducted by ETH Zurich, the Geological Survey of Ethiopia (GSE) and the RiftVolc project, as summarized in Table S1.

<table>
<tr><th>Dataset</th><th>Measured by</th><th>Study</th><th>Survey Area</th><th colspan="2">Average MT site spacing</th><th>Number of MT sites</th><th>Inversion</th></tr>
<tr><td rowspan="3">Local at Aluto</td><td rowspan="3">ETH Zurich & GSE</td><td>Samrock et al. (2015)</td><td rowspan="3">Grid:5 x 15 km</td><td colspan="2" rowspan="3">0.7 km</td><td rowspan="3">165</td><td>ModEM 3-D: $\mathbf{Z}$</td></tr>
<tr><td>Cherkose and Mizunaga (2018)</td><td>ModEM 3-D: $\mathbf{Z}$</td></tr>
<tr><td>Samrock et al. (2020)</td><td>GoFEM 3-D: $\mathbf{\Phi}$</td></tr>
<tr><td>Regional across rift</td><td rowspan="3">RiftVolc Project</td><td>Hübert et al. (2018)</td><td>Profile: 120 km</td><td>4.3 km</td><td rowspan="3">5.9 km</td><td>25</td><td>EMILIA 2D: DET mode</td></tr>
<tr><td rowspan="2">Regional western rift</td><td>-</td><td>Profile: 32 km</td><td>9.6 km</td><td>4</td><td>-</td></tr>
<tr><td>-</td><td>Profile: 51 km</td><td>12.9 km</td><td>4</td><td>-</td></tr>
</table>

Table S1: Information on the MT datasets analyzed in this study. MT data from the surveys of the RiftVolc project are publicly available for download (*Hübert and Whaler*, 2020) as well as ETH survey data (*Samrock et al.*, 2010). Detailed information about the different inversion codes can be found in (*Kelbert et al.*, 2014) (ModEM 3-D) and in (*Kalscheuer et al.*, 2008) (EMILIA 2D).

Text S2.1. Following (*Rung-Arunwan et al.*, 2016), we calculated SSQ-responses over N_s stations to obtain Z^{1D}_{SSQ} (Eq. 7). Further averaging Z^{1D}_{SSQ} over all periods gives a homogeneous model ($\bar{Z}^{1D}_{SSQ}$: Eq. 8). Starting models based on a regional 1-D SSQ-average have been proved to enable successful phase tensor inversion (e.g. *Rung-Arunwan et al.*, 2022).

$$Z_{SSQ}(\mathbf{r},\omega) = \sqrt{(Z_{xx}(\mathbf{r},\omega)^2 + Z_{xy}(\mathbf{r},\omega)^2 + Z_{yx}(\mathbf{r},\omega)^2 + Z_{yy}(\mathbf{r},\omega)^2)/2} \tag{6}$$

$$Z^{1D}_{SSQ}(\omega) = \sqrt[N_s]{\prod_{i=1}^{N_s} Z_{SSQ}(\mathbf{r}_i,\omega)} \tag{7}$$

$$\bar{Z}^{1D}_{SSQ} = \sqrt[N_p]{\prod_{i=1}^{N_p} Z^{1D}_{SSQ}(\omega_i)} \tag{8}$$

$$\rho_{a,SSQ}(\omega) = \frac{|Z_{SSQ}(\omega)|^2}{\omega\mu_0}, \quad \phi_{SSQ}(\omega) = \tan^{-1}\left(\frac{\mathrm{Im}(Z_{SSQ}(\omega))}{\mathrm{Re}(Z_{SSQ}(\omega))}\right) \tag{9}$$

$$\rho^{1D}_{a,SSQ}(\omega) = \frac{|Z^{1D}_{SSQ}(\omega)|^2}{\omega\mu_0}, \quad \phi^{1D}_{SSQ}(\omega) = \tan^{-1}\left(\frac{\mathrm{Im}(Z^{1D}_{SSQ}(\omega))}{\mathrm{Re}(Z^{1D}_{SSQ}(\omega))}\right) \tag{10}$$

$$\bar{\rho}^{1D}_{a,SSQ} = \sqrt[N_T]{\prod_{i=1}^{N_T} \rho^{1D}_{a,SSQ}(\omega_i)}, \quad \bar{\phi}^{1D}_{SSQ} = \sqrt[N_T]{\prod_{i=1}^{N_T} \phi^{1D}_{SSQ}(\omega_i)} \tag{11}$$

The apparent resistivities $\rho_{a,SSQ}$ and phases ϕ_{SSQ} obtained from Z_{SSQ} at each MT site (Eq. 9) and the corresponding regional averages over all sites ($\rho^{1D}_{a,SSQ}, \phi^{1D}_{SSQ}$ from Eq. 10) are shown in Fig. S1.

Text S2.2. Information about the penetration depth z_p of the MT signal comes from the real part of the C-response $\mathrm{Re}(C)$, that we derived from the regional average impedance (Z^{1D}_{SSQ}, Eq. 7). The C-response is a transfer function related to the 1-D impedance by $Z^{1D} = -i\omega\mu_0 C$ and has units of metres. Following *Weidelt* (1972) and *Schmucker and Weidelt* (1975), $2 * \mathrm{Re}(C)$ represents a proxy for the penetration depth at a given period.

$$z_p = 2 * \mathrm{Re}\left(\frac{-\bar{Z}^{1D}_{SSQ}}{i\omega\mu_0}\right), \tag{12}$$

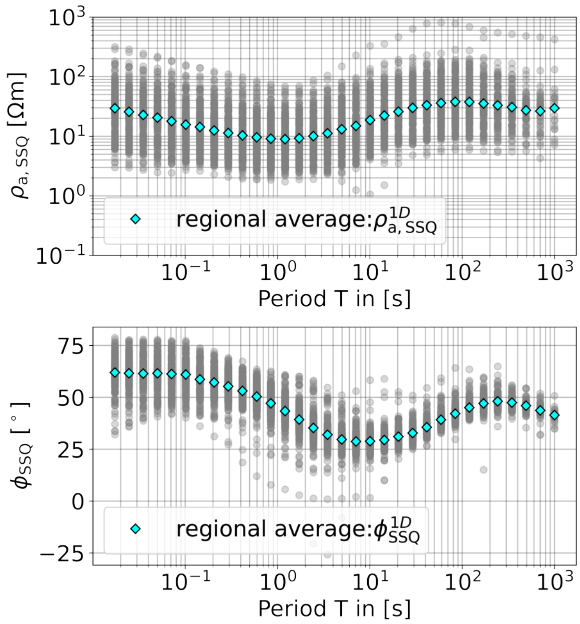

Figure S1: Apparent resistivity ($\rho_{a,SSQ}$) and phases (ϕ_{SSQ}) curves for all stations (gray) and the regional mean values (i.e., $\rho^{1D}_{a,SSQ}$ and $\phi^{1D}_{a,SSQ}$) (blue diamonds).

Additional information about the penetration depth comes from the skin depth z_s, defined as

$$z_s = \sqrt{\frac{2\bar{\rho}^{1D}_{a,SSQ}}{\mu_0 \omega}}. \tag{13}$$

For the periods in our dataset and for the regional mean resistivity, the penetration depth z_p is estimated to be 0.49 km for the shortest and 92.5 km for the longest sounding period (Fig. S2). For the denser station spacing at Aluto ($d_{st} = 0.7\,\mathrm{km}$), the sounding volume overlaps between neighboring sites is given at all periods, whereas outside Aluto area where site spacing is larger ($d_{st} \approx 5.9\,\mathrm{km}$), overlapping sounding volume is given at periods longer than 4.97 s.

Text S2.3. Figure S3 shows roseplot histograms of the geoelectric strike ($\alpha - \beta$) inferred from the phase tensor (Eq. 5) in the western and eastern rift part and at Aluto for different period ranges, along with the orientation from border and Wonji (WFB) faults. As can be seen, the geoelectric strike is in overall good agreement with the geological strike of the local fault systems.

The dominating geoelectric strike over all periods of the entire dataset of this study is about 0° (Fig. S4), hence we did not rotate the data prior to the inversion.

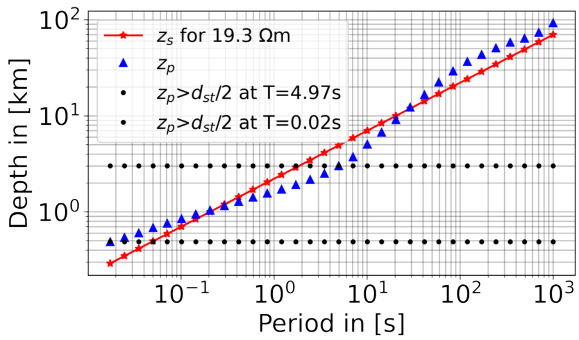

Figure S2: Period-dependent penetration depth z_p (Eq. 12) obtained from Z^{1D}_{SSQ} (Eq. 7) together with the skin depth z_s (Eq. 13) within a homogeneous halfspace of $\bar{\rho}^{1D}_{a,SSQ} = 19.25\,\Omega\,\mathrm{m}$. Horizontal black dotted lines in Fig. S2 mark the minimum period from which z_p exceeds the average site spacing ($d_{st}/2$, Tab S1) at Aluto (0.7 km) and in the profile arms (5.9 km). For this condition ($z_p > d_{st}/2$), sounding volumes of neighbouring stations overlap.

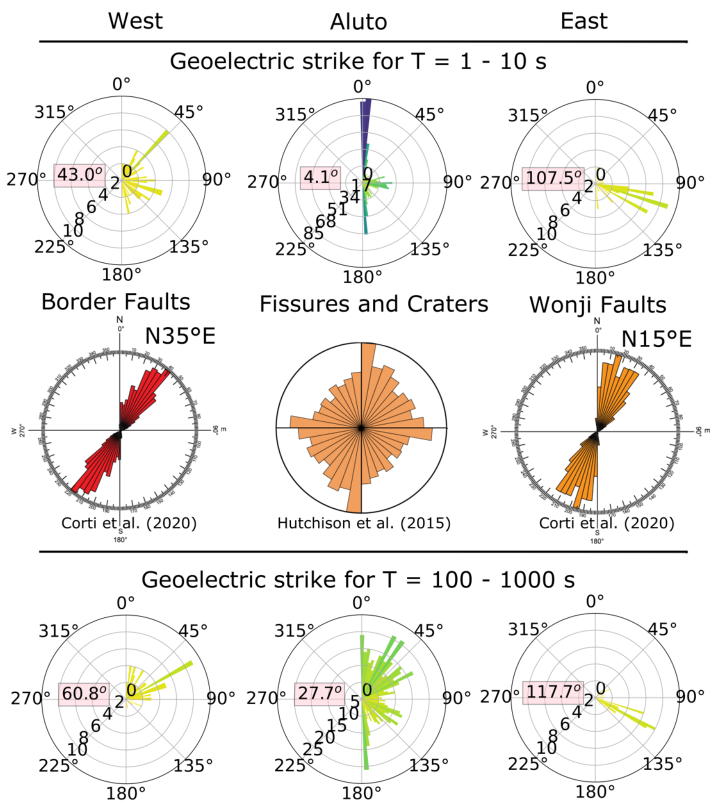

Figure S3: Roseplot histograms of the electric strike direction grouped by different areas within the survey region. Note, the geoelectric strike has a 90° ambiguity (*Caldwell et al.*, 2004). The given angular direction of geoelectric strike corresponds to the direction with the maximum number of counts. Labelled concentric rings indicate the number of data. The geological strike directions of border faults and the WFB are from *Corti et al.* (Fig.7a in 2020), fissure directions and crater alignments at Aluto are from *Hutchison et al.* (Fig.8 in 2015).

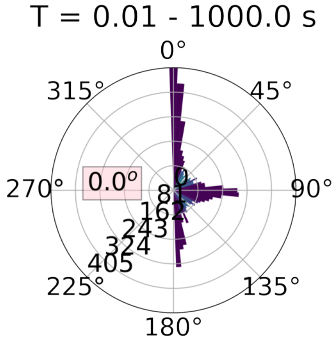

Figure S4: Roseplot histogram of the geoelectric strike ($\alpha - \beta$) inferred from the phase tensor (Eq. 5) for all stations at all frequencies. The given angular direction corresponds to the direction with the maximum number of counts. Ring lines indicate the number of data as given.

Text S3. The MT-dataset of this study clearly demands a 3-D modelling due to 3-D effects observed in the data (Fig. S5). Furthermore, the MT site distribution of our study (see main paper: Fig. 1) requires a multi-scale mesh that would account for the local and the regional site distribution as well as for the varying data resolution.

The mesh we designed for the inversion is shown in Fig. S6. The minimum cell diameters encountered in the mesh are 0.1 km around the site locations at the surface. The cell size increases away from MT stations and with depth to account for the loss of resolution.

Digital Elevation Model given by the NASA SRTM was incorporated into the mesh. This is essential in order to accurately model topography-related galvanic and inductive effects in the data (*Käufl et al.*, 2018).

After topography projection, we assigned a homogeneous resistivity value of $\bar{\rho}^{1D}_{a,SSQ} = 19.25\,\Omega\mathrm{m}$ (Eq. 11) to the subsurface. A data-informed starting model based on the average SSQ impedance (Eq. 10) was shown to be a good choice for data sets with galvanic distortions (*Rung-Arunwan et al.*, 2022).

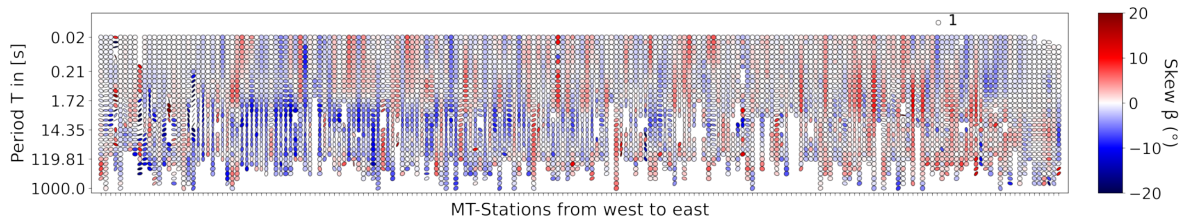

Figure S5: Phase Tensor pseudosection for all stations plotted onto a single line, across the survey area. Phase tensor ellipses were calculated from Eq.5 and are normalized by Φ_{max}. High ellipticities, rapid changes in ellipse main axis directions and high skew values (β) indicate that 3-D effects of the subsurface are present throughout the dataset.

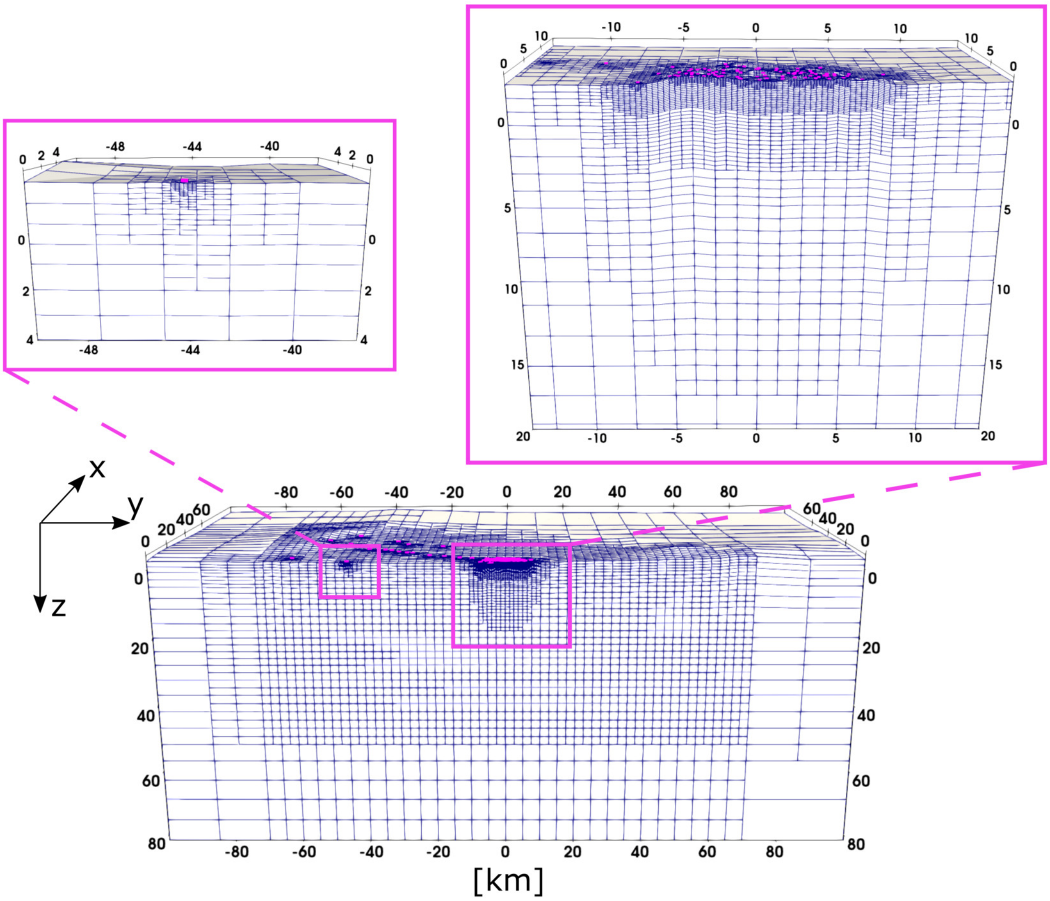

Figure S6: Mesh used in the inversions. The bottom plot shows an EW-slice through the model. The plot on the top left a zoom into a MT site at one of the profile arms, and the plot on the top right a zoom into the mesh at Aluto where a total of 165 MT stations are located. As it is standard in MT the x-axis points to the north, the y-axis to the east and the z-axis is positive downwards.

Text S4. The final model presented in the main paper (Fig. 3) was obtained using a 3-D phase tensor inversion followed by an impedance tensor inversion, whereby the phase tensor model was used as a starting model for the impedance tensor inversion. In the following we present both the phase tensor and impedance tensor models, and provide an in-depth analysis of the data fit for both models.

Text S4.1. Fig. S7 shows the final phase tensor model (corresponding impedance tensor model is shown in Fig. 3 in the main text). We see no major difference between the model in terms of the major large-scale structure. The main features we identified in the impedance tensor model appear equally clear in the phase tensor model: (C1) Aquifer unit, (C2) magma ascent channel, (R1), solidified igneous rock and (C3) lower crustal melt ponding zone.

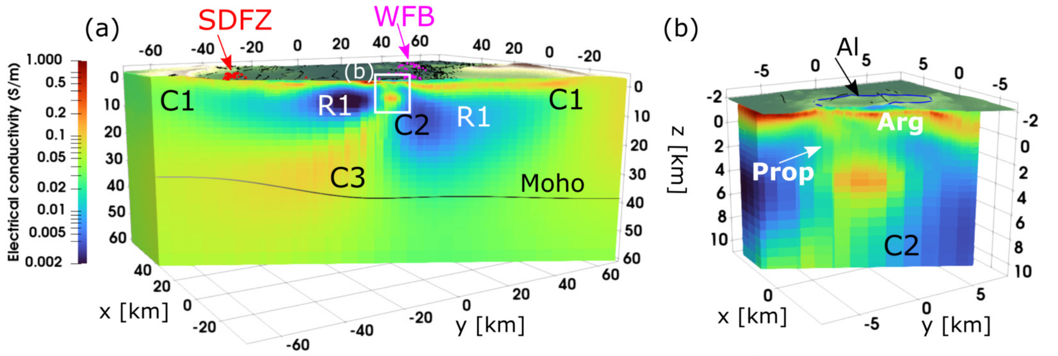

Figure S7: Model obtained from phase tensor inversion. (a) NW-SE oriented profile section, through the obtained model across the entire width of the central MER. The depth of the Moho is taken from (*Stuart et al.*, 2006). Pink and red triangles depict WFB and SDFZ vents respectively. The white box marks the area of the Aluto-Langano geothermal system (b). (b) Close-up of the NW-SE oriented profile section beneath Aluto volcano (Al). Increased conductivities in the shallow subsurface can be attributed to the clay cap formed by argillic alteration (Arg) and higher temperature propyllitic alteration (Prop).

Text S4.2. Pseudosections of the SSQ-averaged apparent resistivities (Fig. S8) and phases (Fig. S9) for the observed and the predicted data of the impedance and the phase tensor model give a qualitative impression of the data fit. Apparent resistivities are generally fitted well by both inversion models, however, absolute values of the impedance tensor model (Fig. S8b) fit the observed data (Fig. S8a) slightly better, compared to apparent resistivity values obtained from the phase tensor model (Fig. S8c). The observed phases are also well fitted by the impedance and the phase tensor model (Fig. S9).

A quantitative measure of the data fit is given by the residuals r and the root-mean-square RMS of observed $\mathrm{F}^{\mathrm{obs}}$ and predicted transfer functions $\mathrm{F}^{\mathrm{pred}}$, where transfer function is either the impedance or phase tensor, depending on the data type that was inverted. The residuals r are defined as follows (see also *Grayver et al.*, 2013):

$$r_i = \frac{\mathrm{F}_\mathrm{i}^{\mathrm{obs}} - \mathrm{F}_\mathrm{i}^{\mathrm{pred}}}{\delta \mathrm{F}_i} \quad \text{with} \quad \mathrm{F} \in [\mathrm{Z}, \Phi], \quad i = 1, ..., N, \tag{14}$$

for N data. $\delta\mathrm{F}$ are the propagated data variances of the observed data with an assigned row-wise error-floor of 5% assigned to the impedance tensor as defined in (*Käufl et al.*, 2020). Data

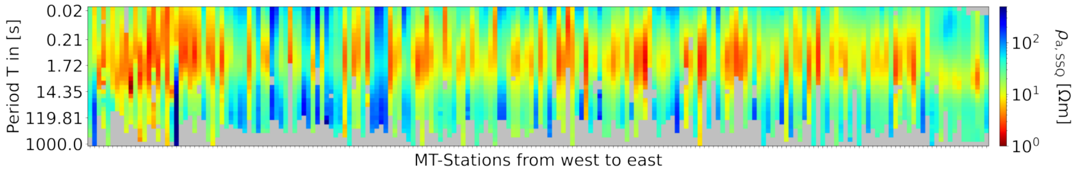

(a) Observed data.

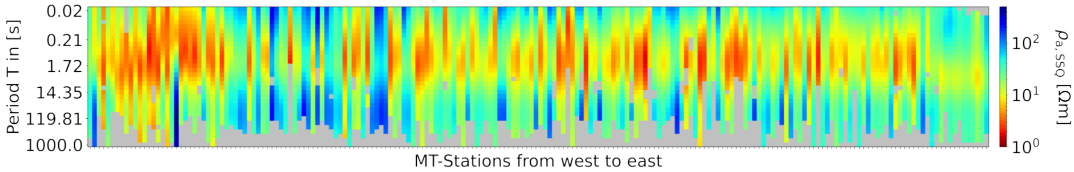

(b) Final model of impedance tensor inversion.

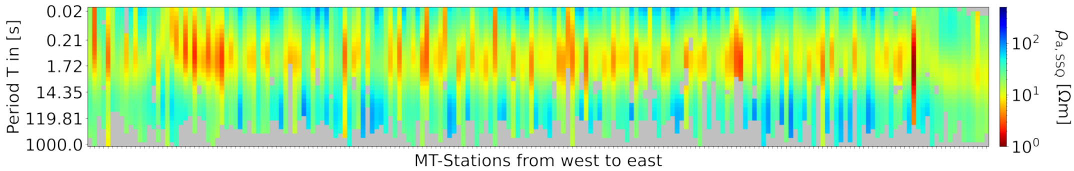

(c) Final model of phase tensor inversion.

Figure S8: Observed and predicted apparent resistivities calculated from $\mathbf{Z}_{SSQ}$ (Eq. 6, Eq. 9) sorted from west to east and projected on the shown "pseudo-profile".

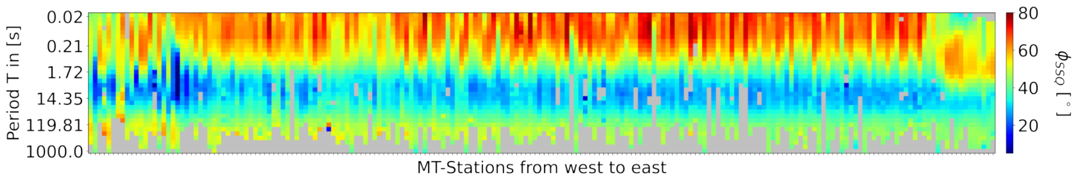

(a) Observed data.

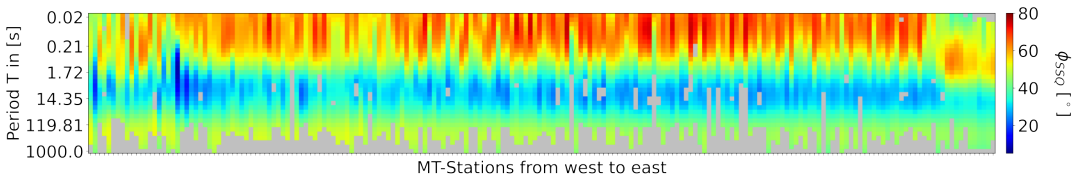

(b) Final model of impedance tensor inversion.

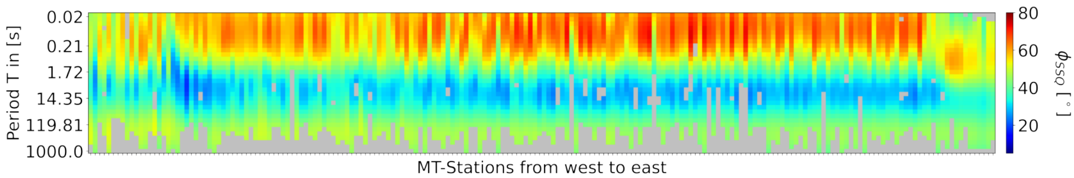

(c) Final model of phase tensor inversion.

Figure S9: Observed and predicted phases calculated from $\mathbf{Z}_{SSQ}$ (Eq. 6, Eq. 9) sorted from west to east and projected on the shown "pseudo-profile".

uncertainties of the phase tensors were obtained by error propagation from the impedance tensor. The RMS is defined as follows:

$$\mathrm{RMS} = \sqrt{\frac{1}{N}\sum_{i=1}^{N} r_i^2} \tag{15}$$

Pseudosections of the RMS-value calculated for all modelled frequencies at all MT-sites are presented for the impedance (Fig. S10a) and the phase tensor (Fig. S10b) models. Both models achieve a good data fit with $(\mathrm{RMS} \leq 1)$ meaning that all data are fitted within the the error bounds at nearly all stations and at all periods.

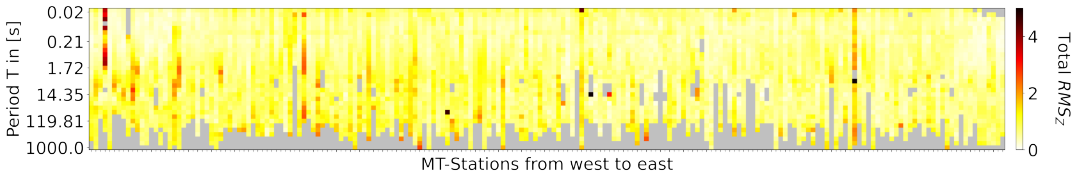

(a) RMS of the impedance tensor model.

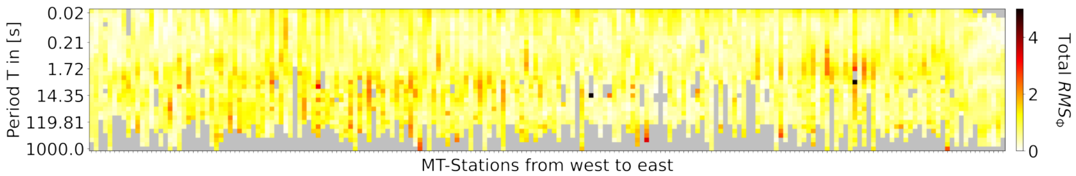

(b) RMS of the phase tensor model.

Figure S10: Achieved RMS of impedance tensor model (a) and phase tensor model (b) presented as pseudosections per MT site and period. Note, that the RMS is always calculated for the respective transfer function used for the inversion (Eq. 14).

Another approach to assess the quality of the fit are crossplots of observed and predicted data (Fig. S11). These crossplots would show a systematic mismatch between observed and predicted data, if a systematic bias exists. Both, apparent resistivities and phase tensor elements, are actually better fitted by the final impedance tensor model (Fig. S11a, Fig. S11b) than by the phase tensor model (Fig. S11c, Fig. S11d). Apparent resistivities calculated from the phase tensor model (Fig. S11c) are less well fitted, reflecting galvanic distortions that are not accounted for in the phase tensor model (see Text S4.3.). It can also be seen that diagonal components of the phase tensor $\Phi_{xx,yy}$ with small magnitudes are generally underestimated (see Fig. S11d).

We conclude that the final impedance tensor model shows an overall good fit of both observed impedance and phase tensors and no systematic mismatch or bias in the data.

Text S4.3. The observed difference in impedance data fit between the final impedance tensor model and the phase tensor model (Fig. S11) is anticipated because: (1) absolute electrical conductivity values are less well constrained in phase tensor inversions compared to impedance tensor inversion (e.g. *Rung-Arunwan et al.*, 2022; *Tietze et al.*, 2015) and (2) the impedance tensors are affected by galvanic distortion, hence the inversion process introduces strong near surface heterogeneities in order to fit distorted responses. This leads to a wider distribution of electrical conductivities recovered by the final impedance tensor model compared to the phase tensor model as illustrated in Fig. S12.

Plane view plots of the surface from both models show that the final impedance tensor model shows a more scattered shallow conductivity structure compared to the phase tensor model (Fig. S13). However, the median of recovered conductivities in both models is identical (Fig. S12). This indicates

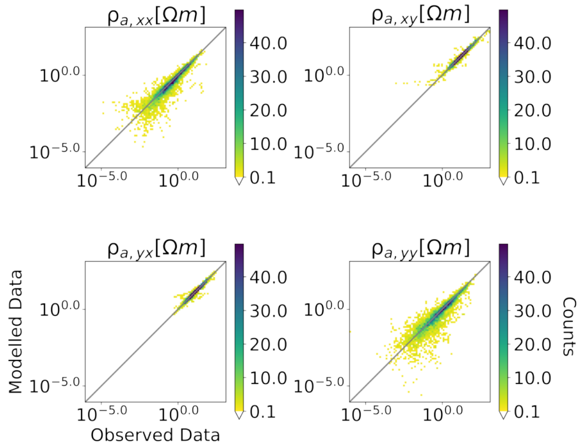

(a) Final model of impedance tensor inversion.

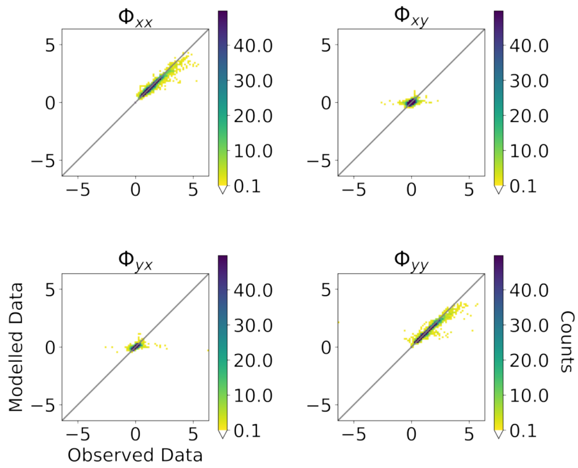

(b) Final model of impedance tensor inversion.

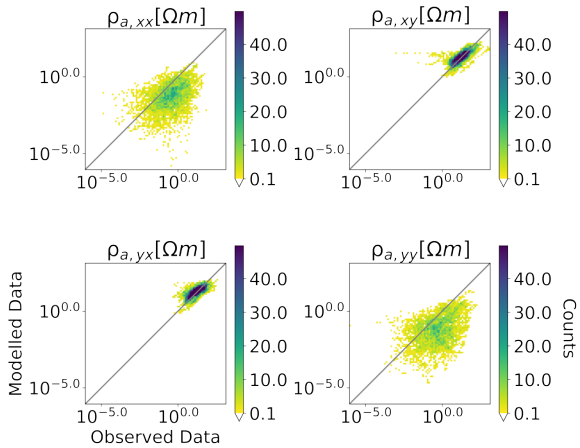

(c) Final model of phase tensor inversion.

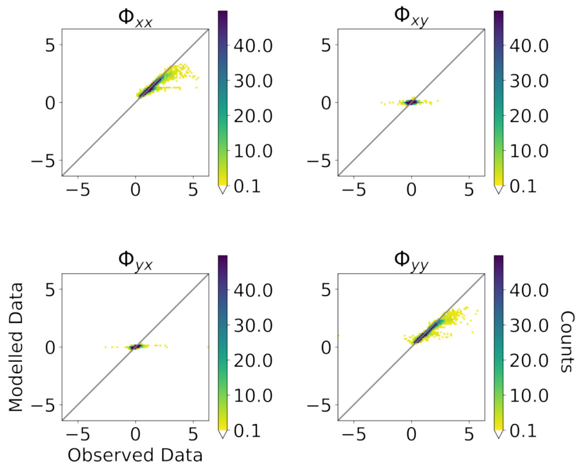

(d) Final model of phase tensor inversion.

Figure S11: Data count crossplots comparing the observed with the predicted apparent resistivity and phase tensors. The gray diagonal line indicates the theoretical distribution for a perfect fit.

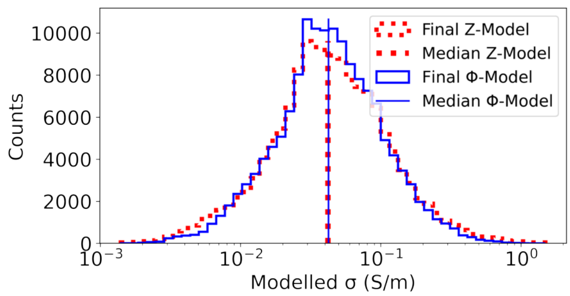

Figure S12: Histogram of predicted conductivities in the final impedance and phase tensor inversion models. Counts refer to the numbers of cells in the mesh with the respective conductivity.

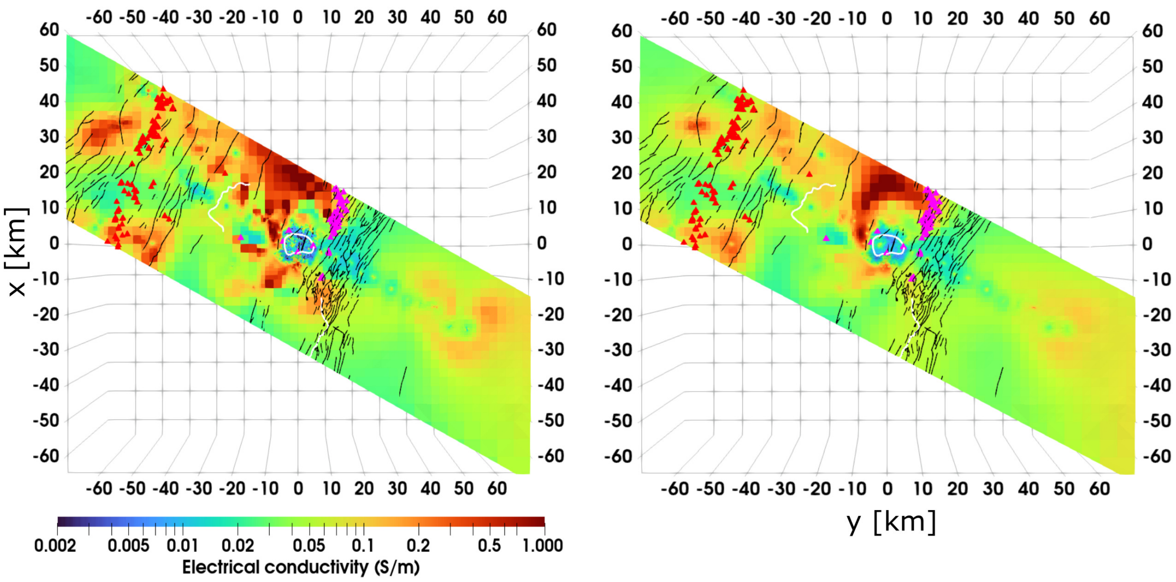

Figure S13: Birdview of the surface from the final model obtained from (a) impedance tensor inversion and from (b) phase tensor inversion. Black lines are fault systems and white lines caldera rims. Triangles are vents in the WFB (magenta) and SDFZ (red).

two important findings: (1) recovered conductivities by the phase tensor inversion are generally in the correct range and (2) impedance tensor inversion only introduces longer tails in the distribution of recovered electrical conductivities, which is due to a need to fit galvanically distorted impedances.

Text S5. The interpretation of recovered electrical conductivities σ_{bulk} in terms of fractions of individual phases present in the considered bulk volume requires knowledge of their electrical conductivities and their degree of connectedness. Magmatic reservoirs and fluid saturated rock are typically described as two-phase systems consisting of a homogeneous rock matrix with conductivity σ_2 and a conducting phase with conductivity σ_1, which is e.g. fluid or magma. For a fully saturated rock, the fraction of the conducting phase χ_1 will be equal to the porosity $\chi_1 = 1 - \chi_2$.

These considerations are summarized in the modified Archies law by (*Glover et al.*, 2000):

$$\sigma_{bulk} = \sigma_1(1-\chi_2)^p + \sigma_2\chi_2^m \quad \text{with} \quad p = \frac{\log(1-\chi_2^m)}{\log(1-\chi_2)}. \tag{16}$$

The degree to which the conducting phase with σ_1 contributes to the bulk electrical conductivity σ_{bulk} depends on its degree of connectedness. A geometrical description of the degrees of connectedness is contained in the cementation component m, which generally increases with the degree of connectedness (*Glover*, 2009). Examples for cementation exponent estimates of end-member geometries are $m = 1$ for a matrix with pores as parallel tubes, $m = 1.5$ for pores in a matrix of closely packed perfect spheres (*Sen et al.*, 1981; *Mendelson and Cohen*, 1982), or $m = 1.15$, which approximates the upper Hashin-Shtrikman bound (*Hashin and Shtrikman*, 1962) and corresponds to the brick-layer model (e.g. *Glover*, 2015).

Text S5.1. In order to relate σ_{bulk} within C3 with basaltic magmatic melt fractions the electrical conductivity of the melt needs to be known under the prevailing conditions. Parameters that predominantly control the electrical conductivity of melt are melt composition, pressure, temperature and the amount of dissolved water within the melt. Estimations of these properties as they are expected to prevail within the lower magmatic ponding zone C3 are summarized in Table S2.

Ni et al. (2011) provides an empirical model that describes the electrical conductivity of basaltic melt for a varying temperature range of $\mathcal{T} = 1200 - 1650\,^\circ\mathrm{C}$ and water content of $c_{H2O}^{melt} = 0.02 - 6.3\,\mathrm{wt\%}$, at a fixed pressure of P=2 GPa (Eq. 17).

$$\log(\sigma) = 2.172 - \frac{860.82 - 204.46\sqrt{c_{H2O}^{melt}}}{\mathcal{T} - 1146.8} \qquad \text{for} \quad \mathcal{T} = 1200 - 1650\,^\circ\mathrm{C}, \quad c_{H2O}^{melt} = 0.02 - 6.3\,\mathrm{wt\%}, \quad P = 2\,\mathrm{GPa} \tag{17}$$

Note, we extrapolated Eq. 17 to lower pressures of P=1 GPa at $\mathcal{T} > 1300\,^\circ\mathrm{C}$. This is justified according to a study from *Tyburczy and Waff* (1983), who have shown that the influence of pressure on the electrical conductivity can be neglected in this $P-\mathcal{T}$-range. A pressure of 1 GPa is equivalent to an estimated lithostatic depth of 36.6 km (Fig. S14) which corresponds to depths of C3 (see e.g. Fig. S7). In accordance with reported conditions from previous studies (Tab. S2) we estimate melt electrical conductivtiy for a temperatures of $\mathcal{T} = 1300 - 1400\,^\circ\mathrm{C}$ and water contents of $c_{H2O}^{melt} = 0.5 - 1\,\mathrm{wt\%}$. Reported water solubility for parental basaltic melt is $c_{H2O}^{melt} <= 1\,\mathrm{wt\%}$ (*Field et al.*, 2013), which is well in the range of maximum water solubility calculated using MagmaSat ($max : c_{H2O}^{melt} = 6.7\,\mathrm{wt\%}$) (*Ghiorso and Gualda*, 2015) for a quarternary basalt collected from a scoria cone NE of Aluto (sample 17-01-05 from *Gleeson et al.*, 2017). Under these conditions electrical conductivities of basaltic melt will lie within $\sigma_2 = 2.86 - 8.41\,\mathrm{S/m}$ (Fig. S15a).

Using modified Archie's law (Eq. 16) we estimated melt fractions for two different cementation exponents ($m = 1.15, 1.5$) and the minimum and maximum electrical conductivity of basaltic melt $\sigma_2 = 2.86 - 8.41\,\mathrm{S/m}$ (see Fig. S15a). The observed bulk electrical conductivity for the conductor C3 is $\sigma_{bulk} = 0.1 - 0.18\,\mathrm{S/m}$ and the electrical conductivity of the surrounding matrix is assumed to be $\sigma_1 = 0.02\,\mathrm{S/m}$. This results in melt fraction of $1.8 - 7.1\,\mathrm{vol.\%}$ and $4.5 - 14.7\,\mathrm{vol.\%}$ for maximum and minimum basaltic melt conductivities respectively (Fig. S15b).

Property	Value	Method	Region	Study
Temperature [°C]	1125-1200	Basaltic melt composition related to T and P	MER	*Ayalew et al.* (2016)
	1400-1460	PRIMELT-2: obtain primary melt composition and temperature	MER	*Rooney et al.* (2012)
Pressure [GPa]	1.01-1.24	Basaltic melt composition related to T and P	MER	*Ayalew et al.* (2016)
	1.5-2.5	Back-correct major element compositions of basalt to $\mathrm{Mg\#72}$	MER: Debre Zeyit	*Rooney et al.* (2005)
Water content [wt%]	0.5 at 0.15 GPa	Thermodynamic modelling with MELTS	MER: Aluto	*Gleeson et al.* (2017)
	1.0 at 0.1 GPa	Thermodynamic modelling with MELTS	MER: Boseti, Gedemsa	*Peccerillo et al.* (2003), *Ronga et al.* (2010)
	0.4-1.0 at 430 MPa	SiO_2 Harker diagrams of experimental vs. measured major elements	NMER: Dabahu volcano, Afar	*Field et al.* (2013)
Partial melt [vol.%]	2-7	Numerical modelling for seismic wave velocities	MER uppermost mantle	*Hammond and Kendall* (2016)
	3-5	P-wave velocity equivalent to study by *Mechie et al.* (1994)	MER low mantle	*Mackenzie et al.* (2005)
	2	Relation of shear wave velocity reduction to melt fraction from *Hammond and Humphreys* (2000)	MER low mantle	*Chambers et al.* (2019)
	≤ 0.6	Relation of shear wave velocity reduction to melt fraction from *Hammond and Humphreys* (2000)	MER mantle	*Gallacher et al.* (2016)
	13	MT study, melt estimation using SIGMELTS	Afar region	*Desissa et al.* (2013)
	≤ 7	Back-correlated $\mathrm{FeO}*$ and SiO_2 contents	MER (DZBJ) Parental mantle melt	*Rooney et al.* (2005)

Table S2: Summary of the results from past studies that constrained prevailing conditions for parental magma generation in the MER. Please note that this list is not comprehensive.

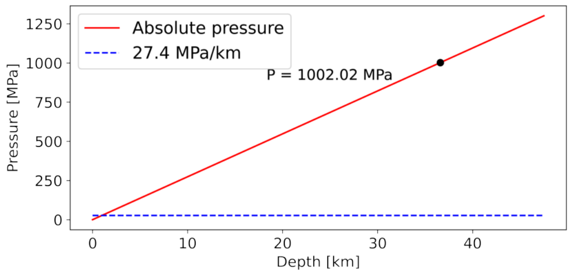

Figure S14: Pressure calculated for a continental crust with $2625\,\mathrm{kg/m^3}$ in a depth of 0-2.5 km and $2800\,\mathrm{kg/m^3}$ for greater depth. These assumptions were reported by *Gleeson et al.* (2017).

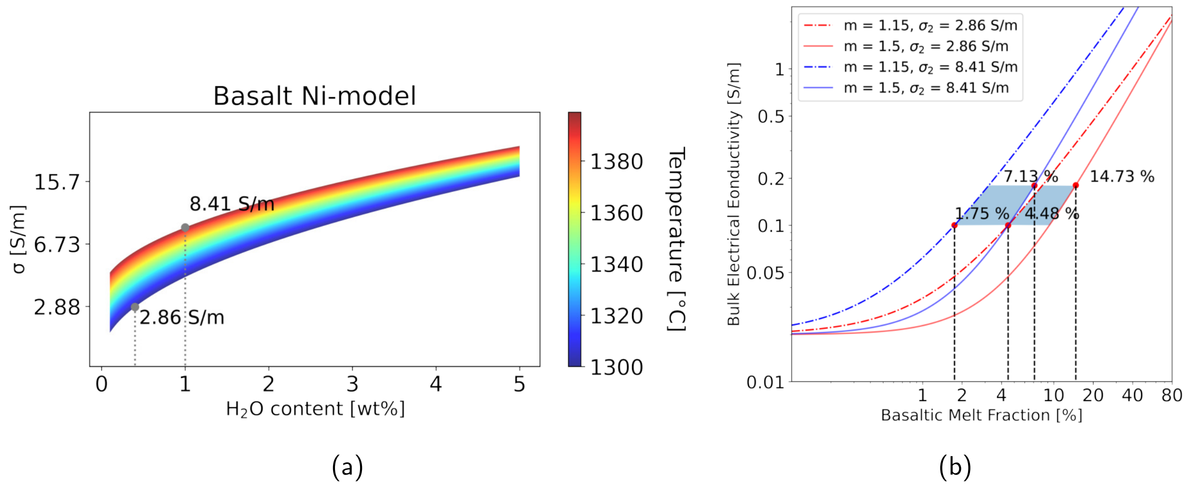

Figure S15: (a) Estimation of σ of basaltic melt after *Ni et al.* (2011) for the given temperature and water content range. (b) Estimation of melt fractions based on the observed bulk electrical conductivities in the lower crustal magma ponding zone using modified Archie's law (Eq. 16). The coloured patches mark the area of observed $\sigma_{bulk} = 0.1 - 0.18\,\mathrm{S/m}$ in the conductor (C3).

Text S5.2. C1 is a prominent electrical conductor that extends at shallow depth over the entire width of the rift (see e.g. Fig. S7). In agreement with the conceptual hydrogeological model of the area by (*Ghiglieri et al.*, 2020) C1 can be interpreted as a fully saturated aquifer system within pyroclastics (ignimbrites) and basalts, where water from the rift shoulders flows into the rift valley.

To verify the interpretation of C1 as an aquifer system with dominating observed bulk conductivities $\sigma_{bulk} = 0.1 - 0.2\,\mathrm{S/m}$ we use modified Archies law (Eq. 16) to estimate the required water fraction within C1. The estimated regional mean electrical conductivity of groundwater is $\sigma_2 = 0.3\,\mathrm{S/m}$ (Fig. S16a).

For the host rock conductivity we assigned $\sigma_1 = 0.05\,\mathrm{S/m}$, which is equivalent to the surrounding rock matrix. The cementation exponent was chosen to be $m = 2.0$, which is in the range of values for sedimentary rocks in upper crustal basins (*Glover et al.*, 2000). Similarly to the estimation of the melt fraction, calculation for estimating the water fraction were perforemd using Eq. 16. Figure S16b shows that a water fraction of $45-79\,\mathrm{vol.\%}$ would be necessary to explain the observed bulk electrical conductivity of $\sigma_{bulk} = 0.1-0.2\,\mathrm{S/m}$. However, such high porosities are unrealistic for a compacted pyroclastic rock (Fig. 6 in *Colombier et al.*, 2017; *Sruoga et al.*, 2004).

Hence, the predicted electrical conductivities cannot be solely explained by ionic conduction in fluid-saturated volcanic rock and suggest that the electrical conductivity of the rock matrix is higher than the assumed $\sigma_2 = 0.05\,\mathrm{S/m}$, possibly due to the presence of electrically conductive clays that form through weathering of ignimbrites.

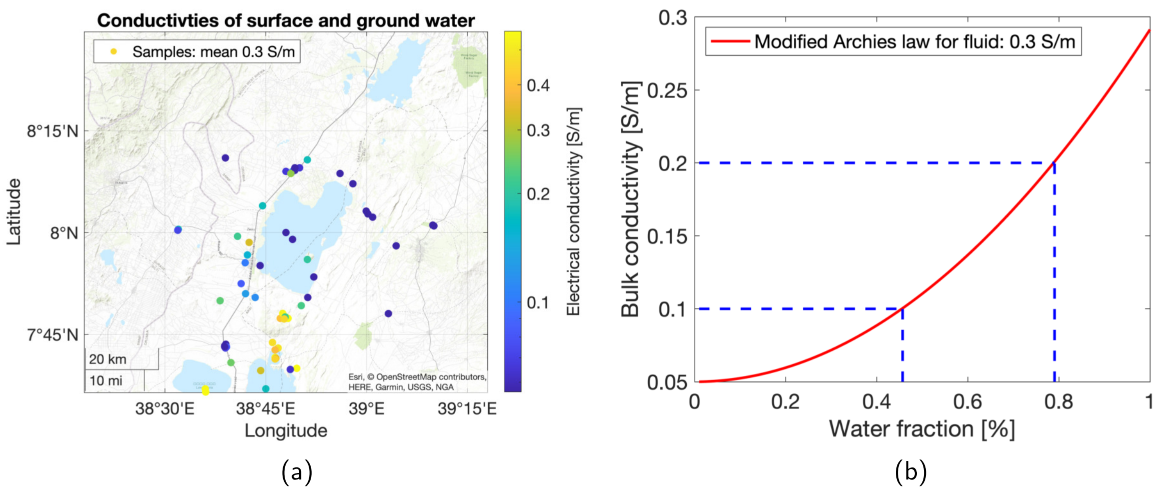

Figure S16: (a) A selection of measured electrical conductivities in the field of surface and groundwaters in the study area, taken from the database of (*Burnside et al.*, 2021). (b) Water fraction present in C1 calculated from the modified Archie's law.

Movie S1. Animation showing a moving profile slice through the final impedance tensor model along with a 0.1 S/m isosurface, that delineates the lower crustal magma ponding zone (C3) and the magma ascent channel (C2), which terminates beneath Aluto volcano. The animation blends into the conceptual model of the central MER also shown in Fig. 6 of the main paper (video file uploaded separately).

References

Ayalew, D., S. Jung, R. L. Romer, F. Kersten, J. A. Pfänder, and D. Garbe-Schönberg (2016), Petrogenesis and origin of modern Ethiopian Rift basalts: Constraints from isotope and trace element geochemistry, *Lithos*, *258-259*, 1–14, 10.1016/j.lithos.2016.04.001.

Burnside, N., N. Montcoudiol, K. Becker, and E. Lewi (2021), Geothermal energy resources in Ethiopia: Status review and insights from hydrochemistry of surface and groundwaters, *Wiley Interdisciplinary Reviews: Water*, p. e1554, 10.1002/wat2.1554.

Caldwell, T. G., H. M. Bibby, and C. Brown (2004), The magnetotelluric phase tensor, *Geophysical Journal International*, *158*(2), 457–469, 10.1111/j.1365-246X.2004.02281.x.

Chambers, E. L., N. Harmon, D. Keir, and C. A. Rychert (2019), Using ambient noise to image the northern East African Rift, *Geochemistry, Geophysics, Geosystems*, *20*(4), 2091–2109, 10.1029/2018GC008129.

Cherkose, B. A., and H. Mizunaga (2018), Resistivity imaging of Aluto-Langano geothermal field using 3-D magnetotelluric inversion, *Journal of African Earth Sciences*, *139*, 307–318, 10.1016/j.jafrearsci.2017.12.017.

Colombier, M., F. B. Wadsworth, L. Gurioli, B. Scheu, U. Kueppers, A. Di Muro, and D. B. Dingwell (2017), The evolution of pore connectivity in volcanic rocks, *Earth and Planetary Science Letters*, *462*(15), 99–109, 10.1016/j.epsl.2017.01.011.

Corti, G., F. Sani, A. A. Florio, T. Greenfield, D. Keir, A. Erbello, A. A. Muluneh, and A. Ayele (2020), Tectonics of the Asela-Langano margin, Main Ethiopian Rift (East Africa), *Tectonics*, *39*(8), 0–2, 10.1029/2020TC006075.

Desissa, M., N. E. Johnson, K. A. Whaler, S. Hautot, S. Fisseha, and G. J. Dawes (2013), A mantle magma reservoir beneath an incipient mid-ocean ridge in Afar, Ethiopia, *Nature Geoscience*, *6*(10), 861–865, 10.1038/ngeo1925.

Field, L., J. Blundy, A. Calvert, and G. Yirgu (2013), Magmatic history of Dabbahu, a composite volcano in the Afar Rift, Ethiopia, *Bulletin*, *125*(1-2), 128–147, 10.1130/B30560.1.

Gallacher, R. J., D. Keir, N. Harmon, G. Stuart, S. Leroy, J. O. Hammond, et al. (2016), The initiation of segmented buoyancy-driven melting during continental breakup, *Nature Communications*, *7*, 1–9, 10.1038/ncomms13110.

Ghiglieri, G., M. Pistis, B. Abebe, T. Azagegn, T. A. Engidasew, D. Pittalis, et al. (2020), Three-dimensional hydrostratigraphical modelling supporting the evaluation of fluoride enrichment in groundwater: Lakes basin (Central Ethiopia), *Journal of Hydrology: Regional Studies*, *32*, 100,756, 10.1016/j.ejrh.2020.100756.

Ghiorso, M. S., and G. A. Gualda (2015), An H_2O–CO_2 mixed fluid saturation model compatible with rhyolite-MELTS, *Contributions to Mineralogy and Petrology*, *169*(6), 1–30, 10.1007/s00410-015-1141-8.

Gleeson, M. L., M. J. Stock, D. M. Pyle, T. A. Mather, W. Hutchison, G. Yirgu, and J. Wade (2017), Constraining magma storage conditions at a restless volcano in the Main Ethiopian Rift using phase equilibria models, *Journal of Volcanology and Geothermal Research*, *337*, 44–61, 10.1016/j.jvolgeores.2017.02.026.

Glover, P. (2009), What is the cementation exponent? A new interpretation, *The Leading Edge*, *28*(1), 82–85, 10.1190/1.3064150.

Glover, P. (2015), Geophysical properties of the near surface Earth: Electrical properties, in *Treatise on Geophysics*, edited by G. Schubert, 2 ed., chap. 11.04, pp. 89–137, Elsevier Oxford, The address of the publisher, 10.1016/B978-0-444-53802-4.00189-5.

Glover, P., M. Hole, and J. Pous (2000), A modified Archie's law for two conducting phases, *Earth and Planetary Science Letters*, *180*(3-4), 369–383, 10.1016/S0012-821X(00)00168-0.

Grayver, A., K. Tietze, and O. Ritter (2013), RMS-Rather Meaningless Simplification?, in *Proceedings on the 25th Schmucker-Weidelt-Kolloquium für Elektromagnetische Tiefenforschung*, pp. 31–35, Kirchhundem Rahrbach, Germany.

Hammond, J. O., and J. M. Kendall (2016), Constraints on melt distribution from seismology: A case study in Ethiopia, *Environmental Geochemistry and Health, With Special Reference to Developing Countries*, *420*(1), 127–147, 10.1144/SP420.14.

Hammond, W. C., and E. D. Humphreys (2000), Upper mantle seismic wave attenuation: Effects of realistic partial melt distribution, *Journal of Geophysical Research, Solid Earth*, *105*(B5), 10,987–10,999, 10.1029/2000JB900042.

Hashin, Z., and S. Shtrikman (1962), A variational approach to the theory of the elastic behaviour of polycrystals, *Journal of the Mechanics and Physics of Solids*, *10*(4), 343–352, 10.1016/0022-5096(62)90005-4.

Hübert, J., and K. Whaler (2020), Magnetotelluric and transient electromagnetic data from the Main Ethiopian Rift. British Geological Survey. (dataset)., 10.5285/2fb02ed4-5f50-4c14-aeec-27ee13aafc38.

Hübert, J., K. Whaler, and S. Fisseha (2018), The electrical structure of the central Main Ethiopian Rift as imaged by magnetotellurics: Implications for magma storage and pathways, *Journal of Geophysical Research, Solid Earth*, *123*(7), 6019–6032, 10.1029/2017JB015160.

Hutchison, W., T. A. Mather, D. M. Pyle, J. Biggs, and G. Yirgu (2015), Structural controls on fluid pathways in an active rift system: A case study of the Aluto volcanic complex, *Geosphere*, *11*(3), 542–562, 10.1130/GES01119.1.

Kalscheuer, T., L. B. Pedersen, and W. Siripunvaraporn (2008), Radiomagnetotelluric two-dimensional forward and inverse modelling accounting for displacement currents, *Geophysical Journal International*, *175*(2), 486–514, 10.1111/j.1365-246X.2008.03902.x.

Käufl, J. S., A. V. Grayver, and A. V. Kuvshinov (2018), Topographic distortions of magnetotelluric transfer functions: A high-resolution 3-D modelling study using real elevation data, *Geophysical Journal International*, *215*(3), 1943–1961, 10.1093/gji/ggy375.

Käufl, J. S., A. V. Grayver, M. J. Comeau, A. V. Kuvshinov, M. Becken, J. Kamm, et al. (2020), Magnetotelluric multiscale 3-D inversion reveals crustal and upper mantle structure beneath the Hangai and Gobi-Altai region in Mongolia, *Geophysical Journal International*, *221*(2), 1002–1028, 10.1093/gji/ggaa039.

Kelbert, A., N. Meqbel, G. D. Egbert, and K. Tandon (2014), ModEM: A modular system for inversion of electromagnetic geophysical data, *Computers Geosciences*, *66*, 40–53, 10.1016/j.cageo.2014.01.010.

Mackenzie, G. D., H. Thybo, and P. K. Maguire (2005), Crustal velocity structure across the Main Ethiopian Rift: Results from two-dimensional wide-angle seismic modelling, *Geophysical Journal International*, *162*(3), 994–1006, 10.1111/j.1365-246X.2005.02710.x.

Mechie, J., K. Fuchs, and R. Altherr (1994), The relationship between seismic velocity, mineral composition and temperature and pressure in the upper mantle—with an application to the Kenya Rift and its eastern flank, *Tectonophysics*, *236*(1-4), 453–464, 10.1016/0040-1951(94)90189-9.

Mendelson, K. S., and M. H. Cohen (1982), The effect of grain anisotropy on the electrical properties of sedimentary rocks, *Geophysics*, *47*(2), 257–263, 10.1190/1.1441332.

Ni, H., H. Keppler, and H. Behrens (2011), Electrical conductivity of hydrous basaltic melts: Implications for partial melting in the upper mantle, *Contributions to Mineralogy and Petrology*, *162*(3), 637–650, 10.1007/s00410-011-0617-4.

Peccerillo, A., M. R. Barberio, G. Yirgu, D. Ayalew, M. Barbieri, and T. W. Wu (2003), Relationships between mafic and peralkaline silicic magmatism in continental rift settings: A petrological, geochemical and isotopic study of the Gedemsa volcano, Central Ethiopian Rift, *Journal of Petrology*, *44*(11), 2003–2032, 10.1093/petrology/egg068.

Ronga, F., M. Lustrino, A. Marzoli, and L. Melluso (2010), Petrogenesis of a basalt-comendite-pantellerite rock suite: the Boseti Volcanic Complex (Main Ethiopian Rift), *Mineralogy and Petrology*, *98*(1-4), 227–243, 10.1007/s00710-009-0064-3.

Rooney, T. O., T. Furman, G. Yirgu, and D. Ayalew (2005), Structure of the Ethiopian lithosphere: Xenolith evidence in the Main Ethiopian Rift, *Geochimica et Cosmochimica Acta*, *69*(15), 3889–3910, 10.1016/j.gca.2005.03.043.

Rooney, T. O., C. Herzberg, and I. D. Bastow (2012), Elevated mantle temperature beneath East Africa, *Geology*, *40*(1), 27–30, 10.1130/G32382.1.

Rung-Arunwan, T., W. Siripunvaraporn, and H. Utada (2016), On the Berdichevsky average, *Physics of the Earth and Planetary Interiors*, *253*, 1–4, 10.1016/j.pepi.2016.01.006.

Rung-Arunwan, T., W. Siripunvaraporn, and H. Utada (2022), The effect of initial and prior models on phase tensor inversion of distorted magnetotelluric data, *Earth, Planets and Space*, *74*(51), 1–24, 10.1186/s40623-022-01611-8.

Samrock, F., A. Kuvshinov, J. Bakker, A. Jackson, S. Fisseha, staff of Addis Ababa University, and the Geological Survey of Ethiopia (2010), Magnetotelluric and vertical magnetic transfer functions acquired at the Aluto-Langano geothermal field, Ethiopia, 10.17611/DP/EMTF/ETHIOPIA/ETHZ, from the IRIS database, `http://ds.iris.edu/spud/emtf`.

Samrock, F., A. Kuvshinov, J. Bakker, A. Jackson, and S. Fisseha (2015), 3-D analysis and interpretation of magnetotelluric data from the Aluto-Langano geothermal field, ethiopia, *Geophysical Journal International*, *202*(3), 1923–1948, 10.1093/gji/ggv270.

Samrock, F., A. V. Grayver, B. Cherkose, A. Kuvshinov, and M. O. Saar (2020), Aluto-Langano geothermal field, Ethiopia: Complete image of underlying magmatic-hydrothermal system revealed by revised interpretation of magnetotelluric data, in *Proceedings World Geothermal Congress (WGC 2020+1)*, p. 11054, Reykjavic, Iceland, 10.3929/ethz-b-000409980.

Schmucker, U., and P. Weidelt (1975), Electromagnetic induction in the Earth, *Lecture Notes, Aarhus Univ., Denmark*.

Sen, P., C. Scala, and M. Cohen (1981), A self-similar model for sedimentary rocks with application to the dielectric constant of fused glass beads, *Geophysics*, *46*(5), 781–795, 10.1190/1.1441215.

Sruoga, P., N. Rubinstein, and G. Hinterwimmer (2004), Porosity and permeability in volcanic rocks: a case study on the Serie Tobífera, South Patagonia, Argentina, *Journal of Volcanology and Geothermal Research*, *132*(1), 31–43, 10.1016/S0377-0273(03)00419-0.

Stuart, G., I. Bastow, and C. Ebinger (2006), Crustal structure of the northern main ethiopian rift from receiver function studies, *Geological Society, London, Special Publications*, *259*(1), 253–267, 10.1144/GSL.SP.2006.259.01.20.

Tietze, K., O. Ritter, and G. D. Egbert (2015), 3-D joint inversion of the magnetotelluric phase tensor and vertical magnetic transfer functions, *Geophysical Journal International*, *203*(2), 1128–1148, 10.1093/gji/ggv347.

Tyburczy, J. A., and H. S. Waff (1983), Electrical conductivity of molten basalt and andesite to 25 kilobars pressure: Geophysical significance and implications for charge transport and melt structure, *Journal of Geophysical Research, Solid Earth*, *88*(B3), 2413–2430, 10.1029/JB088iB03p02413.

Weidelt, P. (1972), The inverse problem of geomagnetic induction, *Journal of Geophysics*, *38*, 257–289, 10.1093/gji/35.1.379.